NASA/CR- *1998* - **207578**

IN 34-CR
077660

NASA Order H-28721D

Rapid Prediction of Unsteady Three-Dimensional Viscous Flows in Turbopump Geometries

Final Report - Year 1
March 21, 1998

Daniel J. Dorney
Department of Mechanical Engineering
1700 West Third Avenue
GMI Engineering & Management Institute
Flint, MI 48504-4898

REPORT DOCUMENTATION PAGE

Public reporting burden for this collection of information is estimated to average 1 hour per response, including the time for reviewing instructions, searching existing data sources, gathering and maintaining the data needed, and completing and reviewing the collection of information. Send comments regarding this burden estimate or any other aspect of this collection of information, including suggestions for reducing this burden, to Washington Headquarters Services, Directorate for Information Operations and Reports, 1215 Jefferson Davis Highway, Suite 1204, Arlington, VA 22202-4302, and to the Office of Management and Budget, Paperwork Reduction Project (0704-0188), Washington, DC 20503.

1. AGENCY USE ONLY (Leave blank)	2. REPORT DATE 03/21/98	3. REPORT TYPE AND DATES COVERED 8/31/97-02/21/98

4. TITLE AND SUBTITLE
Rapid Prediction of Unsteady Three-Dimensional Viscous Flows in Turbopump Geometries

5. FUNDING NUMBERS
H-28721D

6. AUTHORS

Daniel J. Dorney

7. PERFORMING ORGANIZATION NAME(S) AND ADDRESS(ES)

GMI Engineering & Management Institute
Dept. of Mech. Engr., 1700 West Third Ave.
Flint, MI 48504-4898

8. PERFORMING ORGANIZATION REPORT NUMBER

98-2

9. SPONSORING/MONITORING AGENCY NAME(S) AND ADDRESS(ES)

NASA MSFC

Marshall Space Flight Center, AL 35812

10. SPONSORING/MONITORING AGENCY REPORT NUMBER

11. SUPPLEMENTARY NOTES

12a. DISTRIBUTION/AVAILABILITY STATEMENT

12b. DISTRIBUTION CODE

13. ABSTRACT (Maximum 200 words)

A program is underway to improve the efficiency of a three-dimensional Navier-Stokes code and generalize it for nozzle and turbopump geometries. Code modifications have included the implementation of parallel processing software, incorporation of new physical models and generalization of the multiblock capability. The final report contains details of code modifications, numerical results for several nozzle and turbopump geometries, and the implementation of the parallelization software.

14. SUBJECT TERMS

CFD, nozzles, turbopumps, Navier-Stokes

15. NUMBER OF PAGES
56

16. PRICE CODE

17. SECURITY CLASSIFICATION OF REPORT	18. SECURITY CLASSIFICATION OF THIS PAGE	19. SECURITY CLASSIFICATION OF ABSTRACT	20. LIMITATION OF ABSTRACT
unclassified	unclassified	unclassified	UL

Summary

A program is underway to improve the efficiency of a three-dimensional, unsteady, Navier-Stokes code and generalize it for nozzle and turbopump geometries. Code modifications have included the implementation of parallel processing software, incorporation of new physical models and generalization of the multi-block capability to allow the simultaneous simulation of nozzles and turbopumps. The modified code has been applied to relevant nozzle and turbopump configurations.

The following results are described in the 1997 Final Report:

- Details of code modifications

- Numerical results for a nozzle configuration

- Numerical results for interacting nozzle/blade/vane geometries

- Parallelization of the Navier-Stokes code using the Message Passing Interface software

Contents

List of Figures

3

List of Tables

Nomenclature

$\dot{m}$ - Mass flow rate

M - Mach number

P - Static pressure

P_t - Total pressure

S - Entropy

T - Static temperature

T_t - Total temperature

W - Work

α - Absolute frame circumferential flow angle

β - Relative frame circumferential flow angle

η - Efficiency

ϕ - Absolute frame radial flow angle

ψ - Relative frame radial flow angle

SUBSCRIPTS

in   - Inlet

out   - Exit

ts   - Total-to-static

tt   - Total-to-total

∞ - Free stream

SUPERSCRIPTS

$\sim$ - Relative frame quantity

Introduction

Flow unsteadiness is a major factor in turbine performance and durability. This is especially true if the turbine is a high work design, compact, transonic, supersonic, counter rotating, or uses a dense drive gas. The vast majority of modern rocket turbine designs fall into these categories. For example, the (Space Transportation Main Engine) STME fuel turbine, a high work, transonic design, was found to have an unsteady interrow shock which reduced efficiency by 2 points and increased dynamic loading by 24 percent. The Revolutionary Reusable Technology Turbopump (RRTT), which uses full flow oxygen for its drive gas, was found to shed vortices with such energy as to raise serious blade durability concerns. In both cases, the sources of the problems were uncovered (before turbopump testing) with the application of validated, unsteady computational fluid dynamics (CFD) to the designs. In the case of the RRTT and the Alternate Turbopump Development (ATD) turbines, the unsteady CFD codes have been used not just to identify problems, but to guide designs which mitigate problems due to unsteadiness. Using unsteady flow analyses as a part of the design process will lead to turbine designs with higher performance (which effects temperature and mass flow rate) and fewer dynamics problems. One drawback to three-dimensional unsteady flow analyses, however, is that computation times are often on the order of weeks or months. This time scale does not allow for parametric design studies. The objective of the current program is to generalize and improve the efficiency of a three-dimensional, unsteady, Navier-Stokes code.

Code Improvements

The following improvements have been made to the CORSAIR analysis during the last quarter:

- A parallel version of the flow analysis has been developed using the Message Passage Interface (MPI) software.

- The inlet boundary conditions have been modified to allow the modelling of discrete nozzles. This is accomplished by applying the boundary conditions on a point-wise basis. The inlet boundary conditions can now be specified to be solid wall, subsonic inflow or supersonic inflow. Presently, it is assumed that the nozzles are circular or elliptical in shape. It should be noted that the turbulence quantities are still being calculated based on the airfoil and endwall surfaces. Eventually, the solid wall portions of the inlet should also be used to influence the turbulence quantities.

- The technique for specifying the initial flow field in nozzle simulations has been modified. For normal blade row calculations flow quantities are linearly interpolated between the inlet and exit. In nozzle simulations (where it is assumed that the throat is choked) the flow quantities are interpolated between the inlet and the throat, and

again between the throat and the exit. Note that for choked flow the throat quantities are known, and the area ratio can be used to check the Mach number at the inlet. Application of this technique has been shown to reduce the CPU time by more than 50% compared to initializing the flow field by interpolating the flow quantities between the inlet and exit.

- A low-memory version of the code has been written in which many of the subroutines not necessary for nozzle simulations have been eliminated. This, in turn, has allowed the elimination of considerable branching logic. For a given problem size the low-memory version of the requires 40% less memory, and is 30% faster, than the standard analysis for nozzle simulations

- PLOT3D files can now be specified to be formatted or unformatted.

- A subroutine to mass average the flow quantities at the inlet and exit of each blade row has been added to the analysis to complement the existing area-averaging subroutine.

- A comprehensive and updated version of the CORSAIR User's Manual has been completed.

Numerical Simulations

FASTRAC Nozzle Operating in RP1

The relevant turbine nozzle geometry in this investigation is from the FASTRAC program [1]. Two views of the nozzle grid (constant i- and constant k-planes, respectively) are shown in Figs. 1 and 2. The computational grid contains 131 points in the streamwise (i) direction, 81 grid points in circumferential (j) direction and 21 points in the radial (k) direction. Thus, the computational grid contains a total of 222,831 grid points. The nozzle is designed to have an inlet Mach number of $M_1 \approx 0.23$ and an exit Mach number of $M_2 \approx 2.13$. The inlet static temperature is $1595° R$ and the ratio of specific heats is $\gamma = 1.108$. The Reynolds number was set at $Re = 1 \times 10^6$.

Mach number contours at the inlet and exit of the nozzle are shown in Figs. 3 and 4, respectively. The average Mach number in the inlet plane is approximately $M_1 = 0.23$, which is in excellent agreement with the design intent. The average Mach number in the exit plane is approximately $M_2 = 2.18$, which compares favorably with the design intent. Figures 5 thru 9 illustrate Mach contours along radial sections of the nozzle, beginning near the centerline and progressing towards the outer casing. These figures indicate that the highest Mach numbers are located near the centerline. Closer to the outer casing (Figs. 8 and 9) the Mach number decreases due to the endwall boundary layer. Figure 10, which shows Mach contours in a circumferential ($j = 20$) plane, highlights the thickening of the endwall boundary layer downstream of the throat.

The predicted nozzle loss, which is defined as

$$\omega = \frac{Pt_{inlet} - Pt_{exit}}{Pt_{inlet}} \qquad (1)$$

was $\omega = 0.048$ using the third-order accurate upwind scheme [2, 3]. It is interesting to note that repeating the calculation using a second-order accurate upwind scheme the predicted loss was $\omega = 0.061$. Although the losses differed with order of accuracy, the average inlet/exit Mach numbers and flow patterns were similar.

FASTRAC Nozzle Operating in Nitrogen

A second simulation was performed using nitrogen instead of RP1 as the operating fluid. Operating in nitrogen, the nozzle is designed to have an inlet Mach number of $M_1 \approx 0.23$ and an exit Mach number of $M_2 \approx 2.40$. The inlet static temperature is $523°$ R and the ratio of specific heats is $\gamma = 1.467$. Again, the Reynolds number was set at $Re = 1 \times 10^6$. The grid topology is identical to that used in the RP1 simulation.

Mach number contours at the inlet and exit of the nozzle are shown in Figs. 11 and 12, respectively. The average Mach number in the inlet plane is approximately $M_1 = 0.22$, which agrees closely with the design intent. The average Mach number in the exit plane is approximately $M_2 = 2.42$, which compares favorably with the design intent. Figures 13 thru 17 illustrate Mach contours along radial sections of the nozzle, beginning near the centerline and progressing towards the outer casing. Qualitatively, the results are similar to those predicted in the RP1 simulation. Figure 18, which shows Mach contours in a circumferential ($j = 20$) plane, highlights the endwall boundary layer development downstream of the throat.

The predicted loss using the third-order accurate scheme is $\omega = 0.071$, which is higher than in the RP1 simulation. Repeating the analysis with the second-order accurate scheme the losses were predicted to be $\omega = 0.077$

FASTRAC Nozzle/Blade/Vane Geometry Operating in RP1

A series of numerical simulations have been performed for the FASTRAC turbine configuration consisting of a modelled nozzle exit, a rotor row and a vane row. The actual configuration consists of 26 nozzles, 147 rotor airfoils and 75 vane airfoils. In the current effort, two blade count approximations have been tested:

1. 1-nozzle/6-rotors/3-vanes - Using this approximation it is assumed that there are 150 rotor airfoils, and the rotors are scaled by 147/150 to maintain the pitch-to-chord ratio. The modelling of the nozzle is then exact because 6 rotor passages will completely encompass one nozzle.

Grid Type	Inlet (Nozzle)	Rotor	Vane
O	–	6x91x21x31	3x91x21x31
H	1x14x51x31	6x64x21x31	3x82x31x31
Total Points	22,134	605,430	414,129

Table 1: Grid dimensions for the 1-nozzle/6-rotor/3-vane simulation.

Grid Type	Inlet (Nozzle)	Rotor	Vane
O	–	2x91x21x31	1x91x21x31
H	1x14x51x31	2x64x21x31	1x82x31x31
Total Points	22,134	201,810	138,043

Table 2: Grid dimensions for the 1-nozzle/2-rotor/1-vane simulation.

2. 1-nozzle/2-rotors/1-vane - This scaling also assumes there are 150 rotor airfoils, however the nozzles now are approximated as a continuous slit around the annulus (see Fig. 19).

The grid densities (number of passages$\times$i$\times$j$\times$k) for the two simulations are presented in Tables 1 and 2, respectively. The total number of grid points in the 1-nozzle/6-rotor/3-vane simulation is 1,041,693, while 361,987 grid points are being used in the 1-nozzle/2-rotor/1-vane calculation. Figures 20 and 21 illustrate $(x - y)$ and $(z - y)$ views of the grid used in the 1-nozzle/2-rotor/1-vane simulation. The average value of y^+, the non-dimensional distance of the first grid line above the surface was approximately 1.5 for the airfoils surfaces and 5.0 for the endwall surfaces. A value of $y^+ \approx 5.0$ indicates that increased spanwise grid resolution may be needed.

The turbine is designed to have an inlet Mach number of $M_1 \approx 2.11$. The inlet static temperature is 1291° R and the ratio of specific heats is $\gamma = 1.108$. The Reynolds number was set at $Re = 1.4 \times 10^6$. The results described below are for the 1-nozzle/2-blade/1-vane simulation, which has completed 16 global cycles. A global cycle refers to two rotor airfoils passing one vane airfoil.

Fifty snapshots of the turbine flow field were recorded during the course of one global cycle for the purpose of making an animation. Figures 22 thru 26 show instantaneous Mach number contours at 0%, 20%, 40%, 60% and 80% of a global cycle, respectively. Figures 27 to 31 illustrate instantaneous static pressure contours at the same 5 time increments, while Figs. 32 thru 36 show instantaneous entropy contours. Note that the small breaks in the contour lines at the zonal boundaries are due to limitations in the graphics package and not to interpolation errors in the flow analysis. The graphics package included in the flow analysis first plots the contour lines on the H-grid, then "blanks" out the appropriate portion and

plots the O-grid contours. Thus, the H- and O-grid contours are generated independently. Based on the snapshots of the flow field shown in Figs. 22 to 36 the following observations have been made:

- The absence of strong shock or expansion waves far upstream of the rotor suggest that the rotor is operating at the unique incidence condition.

- There is a detached bow shock which stands approximately 3-4% of the rotor axial chord upstream of the rotor leading edge. The shock extends into the suction side of the rotor passage where it interacts with airfoil the boundary layer. The shock/boundary layer interaction induces flow separation at approximately 15% of the axial chord on the rotor suction surface.

- The separated flow region on the rotor suction surface extends axially to the trailing edge of the airfoil and circumferentially to almost mid-passage (also see Fig. 37). The flow within the separated region is subsonic, but the flow in the remainder of the passage is supersonic. The entropy contours indicate there is a significant amount of loss generation associated with the separated flow region.

- There is minimal unsteady interaction between the rotor and vane airfoils because of the relatively large axial gap between them.

- The flow along the suction surface of the vane stays attached until immediately upstream of the trailing edge. There is a shallow separation bubble originating from the leading edge of the pressure surface and extending to approximately 30% of the axial chord (also see Fig. 38).

- There is a normal shock at approximately 53% of the axial chord on the suction surface of the vane. The shock extends a maximum of about 25% of the distance across the vane passage; the flow does not choke at any time during the course of a global cycle.

In an effort to understand the development of the losses within turbine, instantaneous total pressure contours were plotted in axial planes 30% of the rotor axial chord upstream of the rotor passage, midway between the rotor and vane passages, and 47% of the vane axial chord downstream of the vane (see Figs. 39 to 41). Note that the free stream value of the non-dimensional total pressure is $Pt/P_\infty = 9.12$ (see Table 3). Upstream of the rotor the contours indicate the presence of relatively thick endwall boundary layers (see Fig. 39). The reason for the thickness of the boundary layers is probably two-fold: 1) the solid wall portions of the nozzle at the inlet are located adjacent to the endwalls, and 2) the spanwise grid density needs to be increased. To address the problem of spanwise grid density requirements, a simulation has been initiated using the same streamwise and circumferential grid point distributions, but with 51 spanwise planes instead of 31 spanwise planes. Moving downstream to the region between the rotor and vane it is observed that the total pressure is only about 10-20% of its upstream value (see Fig. 40). There are two regions of low total

Variable	INLET	ROTOR	VANE
M_{in}	2.11	1.93	0.65
$\tilde{M}_{in}$	2.11	1.38	0.65
M_{out}	1.93	0.65	0.39
$\tilde{M}_{out}$	1.93	0.71	0.39
Tt_{in}	1601° R	1598° R	1453° R
$\tilde{T}t_{in}$	1601° R	1469° R	1453° R
Tt_{out}	1598° R	1453° R	1447° R
$\tilde{T}t_{out}$	1598° R	1468° R	1447° R
$(Pt/P_\infty)_{in}$	9.12	7.91	1.51
$(\tilde{P}t/P_\infty)_{in}$	9.12	3.20	1.51
$(Pt/P_\infty)_{out}$	7.91	1.51	1.42
$(\tilde{P}t/P_\infty)_{out}$	7.91	1.74	1.42
α_{in}	72.0°	73.7°	-8.3°
β_{in}	72.0°	69.0°	-8.3°
α_{out}	73.7°	-8.3°	-6.6°
β_{out}	73.7°	-36.0°	-6.6°
ϕ_{in}	0.0°	-8.6°	-3.2°
ψ_{in}	0.0°	-5.0°	-3.2°
ϕ_{out}	-8.6°	-3.2°	-1.3°
ψ_{out}	-8.6°	-0.8°	-1.3°
$\dot{m}$ (lb_m/sec)	7.95	7.98	7.90
W (BTU/lb_m)	–	89.4	–
η_{tt}	–	0.575	–
η_{ts}	–	0.508	–

Table 3: Area-averaged flow quantities - high flow.

pressure associated with the rotor wakes, but also two regions near the shroud endwall where the total pressure is significantly higher. The source of these high total pressure regions is currently under investigation. Downstream of the vane there are loss regions associated with the vane wake and the endwall boundary layers (see Fig. 41).

Table 3 contains the circumferentially and radially area-averaged flow variables at the inlet and exit of each blade row. Note that at the inlet only the flow coming through the nozzle, and not the solid wall values, are included in the average. Based on the interrogation of the solution, it was determined that the mass flow rate had to be reduced to match the intended design-flow conditions. The mass-flow was too high in the first simulation because the limited spanwise grid density resulted in a modelled nozzle that was slightly too large.

12

Variable	INLET	ROTOR	VANE
M_{in}	2.11	1.90	0.45
$\tilde{M}_{in}$	2.11	1.33	0.45
M_{out}	1.90	0.45	0.39
$\tilde{M}_{out}$	1.90	0.78	0.39
Tt_{in}	$1601^\circ\ R$	$1595^\circ\ R$	$1434^\circ\ R$
$\tilde{T}t_{in}$	$1601^\circ\ R$	$1470^\circ\ R$	$1434^\circ\ R$
Tt_{out}	$1595^\circ\ R$	$1434^\circ\ R$	$1430^\circ\ R$
$\tilde{T}t_{out}$	$1595^\circ\ R$	$1465^\circ\ R$	$1430^\circ\ R$
$(Pt/P_\infty)_{in}$	9.12	7.40	1.45
$(\tilde{P}t/P_\infty)_{in}$	9.12	3.00	1.45
$(Pt/P_\infty)_{out}$	7.40	1.45	1.42
$(\tilde{P}t/P_\infty)_{out}$	7.40	1.82	1.42
α_{in}	72.0°	73.8°	-18.5°
β_{in}	72.0°	69.4°	-18.5°
α_{out}	73.8°	-18.5°	-8.6°
β_{out}	73.8°	-61.0°	-8.6°
ϕ_{in}	0.0°	3.7°	1.3°
ψ_{in}	0.0°	-6.0°	1.3°
ϕ_{out}	3.7°	1.3°	-1.2°
ψ_{out}	3.7°	6.2°	-1.2°
$\dot{m}\ (lb_m/sec)$	7.09	7.01	7.16
$W\ (BTU/lb_m)$	–	104.2	–
η_{tt}	–	0.644	–
η_{ts}	–	0.612	–

Table 4: Area-averaged flow quantities - design flow.

Therefore, a simulation was performed in which the nozzle semi-minor axis was adjusted so that the mass flow accurately reflected the design intent. Table 4 contains the circumferentially and radially area-averaged flow variables at the inlet and exit of each blade row at the design-flow conditions.

FASTRAC Nozzle/Blade/Vane Geometry Operating in Nitrogen

A 1-nozzle/2-rotor/1-vane simulation of the turbine (described above) using nitrogen as the operating fluid has been initiated. Th solution has completed one global cycle.

Implementation of Parallel Processing Software

A parallel version of the flow analysis has been developed using the Message Passing Interface (MPI) software. The following logic has been utilized in the parallel analysis:

- A blade passage is defined as the combination of the O-grid, H-grid and clearance grid (if applicable) used to discretize a region of the flow.

- Depending on the number of processors available the problem is decomposed in the following manner:

  - if the number of processors available is greater than the number of blade passages, then the problem is decomposed on a passage-by-passage basis
  - if the number of processors available is greater than the number of blade rows, but less than the number of blade passages, then the problem is decomposed on a row-by-row basis
  - if the number of processors is less than the number of blade rows, then the problem is decomposed into blocks of rows

- The grid and restart files are read on each processor.

- Each processor solves its given portion of the problem.

- After each iteration the processors exchange boundary condition information.

- After each processor completes its given portion, the appropriate information is communicated back to the master process.

- The grid and restart files are reconstructed, and the data is post-processed.

Parallel simulations have been performed for two test cases: 1) a coarse-grid 2-vane/1-rotor/1-stator geometry in which the grid point densities in the different passages were well-balanced (Case 1), and 2) the 1-nozzle/2-rotor/1-vane geometry described above (Case 2), in which the grid point densities were not optimally balanced. The predicted results in for both cases were compared to the results obtained with the serial version of the analysis to verify the accuracy of the solutions. Table 5 contains initial timings obtained using the parallel version of the flow analysis.

Conclusions

A three-dimensional, unsteady, Navier-Stokes code has been generalized for nozzle and turbopump geometries. Code modifications have included the implementation of parallel processing software, the incorporation of new physical models and generalization of the multi-block capability. The modified code has been applied to relevant nozzle and turbopump configurations.

14

Case	Number of Processors	Speed-up
1	4	3.27
2	3	1.70

Table 5: Initial CPU times using the parallel version of the code.

Acknowledgements

The author would like express sincere thanks to Dr. Karen Gundy-Burlet of NASA Ames Research Center for assistance in implementing the MPI protocols into the flow analysis.

References

[1] Griffin, Lisa, Private Communication, September, 1997.

[2] Dorney, D. J., "Rapid Prediction of Unsteady Three-Dimensional Viscous Flows in Turbopump Geometries - Progress Report 1," October 31, 1997.

[3] Dorney, D. J., "Rapid Prediction of Unsteady Three-Dimensional Viscous Flows in Turbopump Geometries - Progress Report 2," January 21, 1998.

[4] http://www.mcs.anl.gov/mpi/mpich

[5] http://scv.bu.edu/SCV/Tutorials/MPI
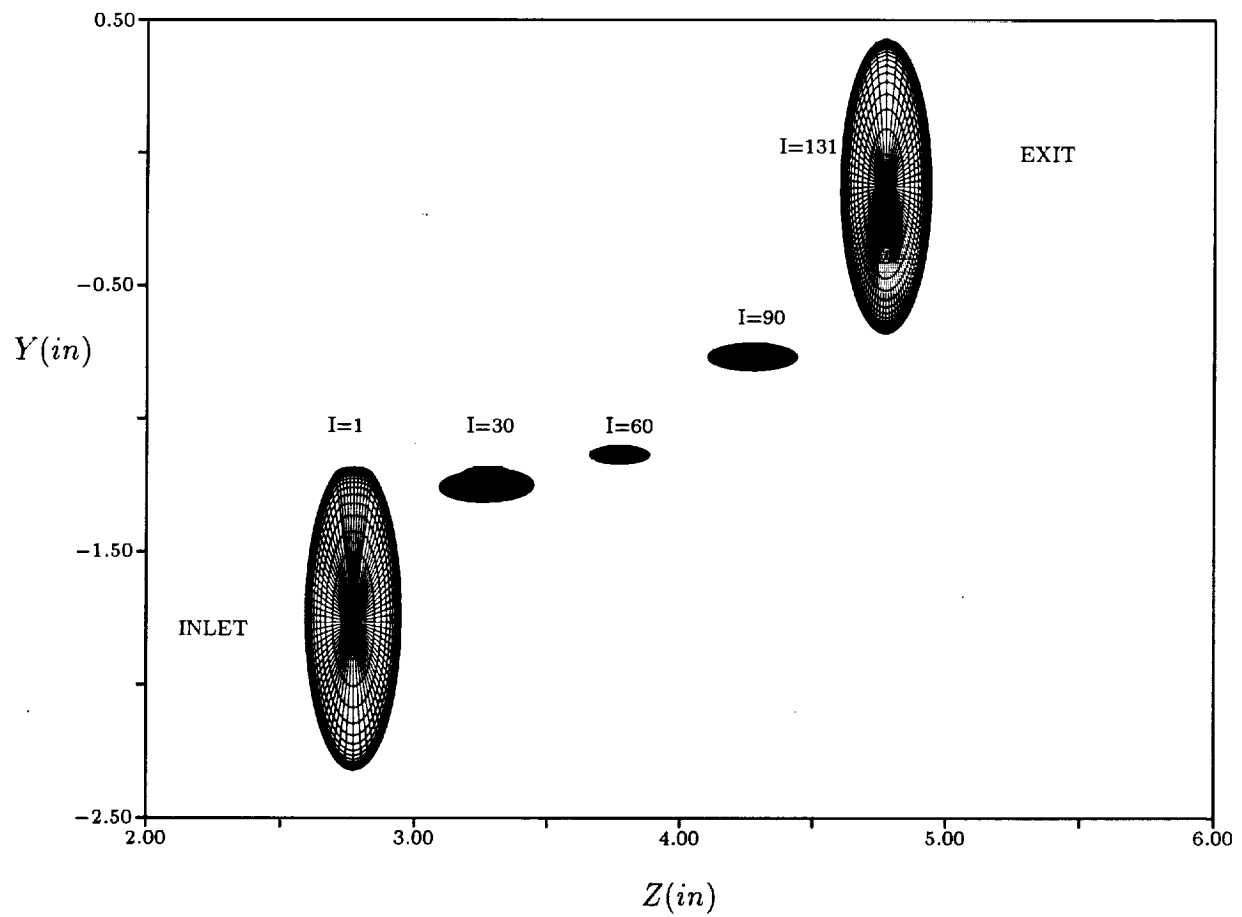
Figure 1: Constant i-plane views of the FASTRAC turbine nozzle.
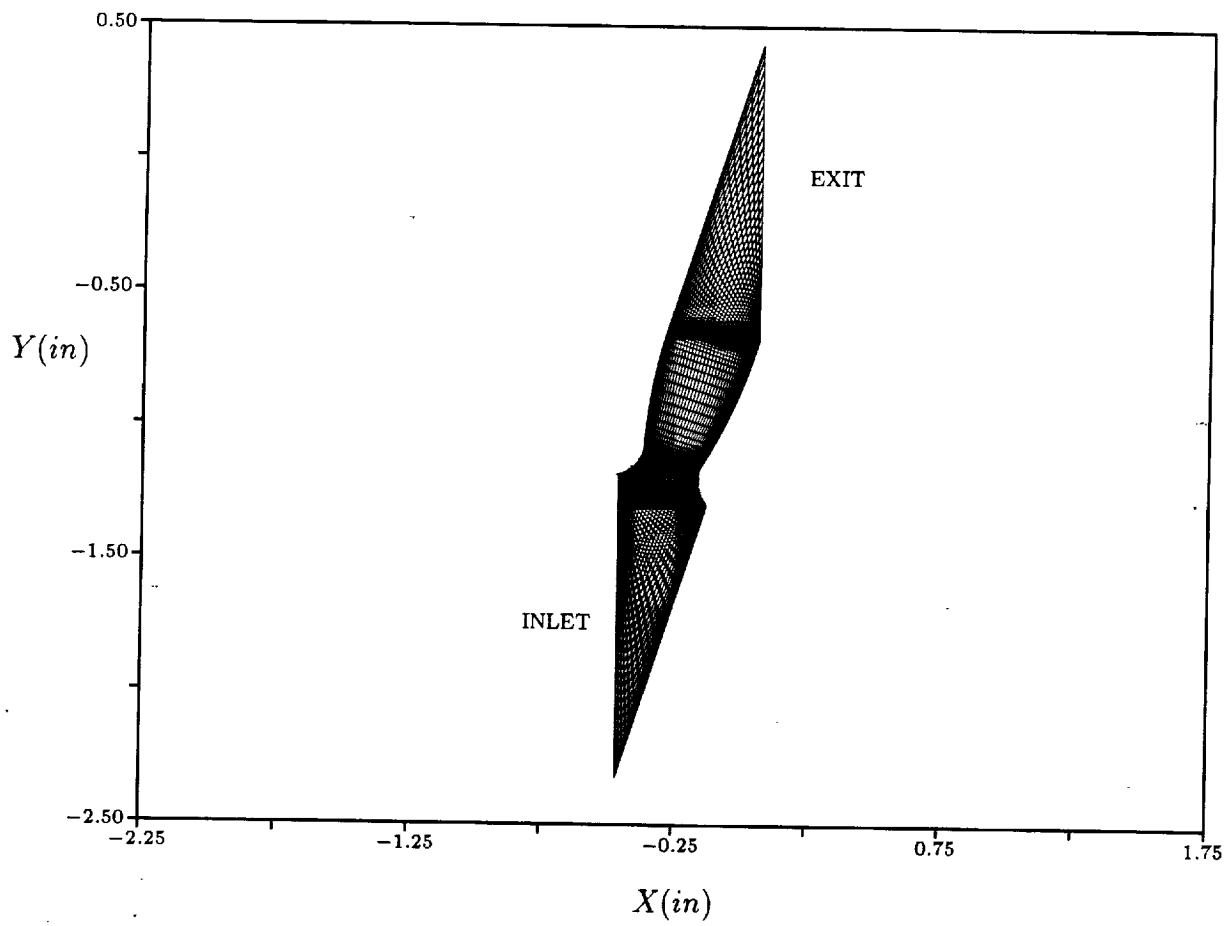
Figure 2: Constant k-plane view of the FASTRAC turbine nozzle.
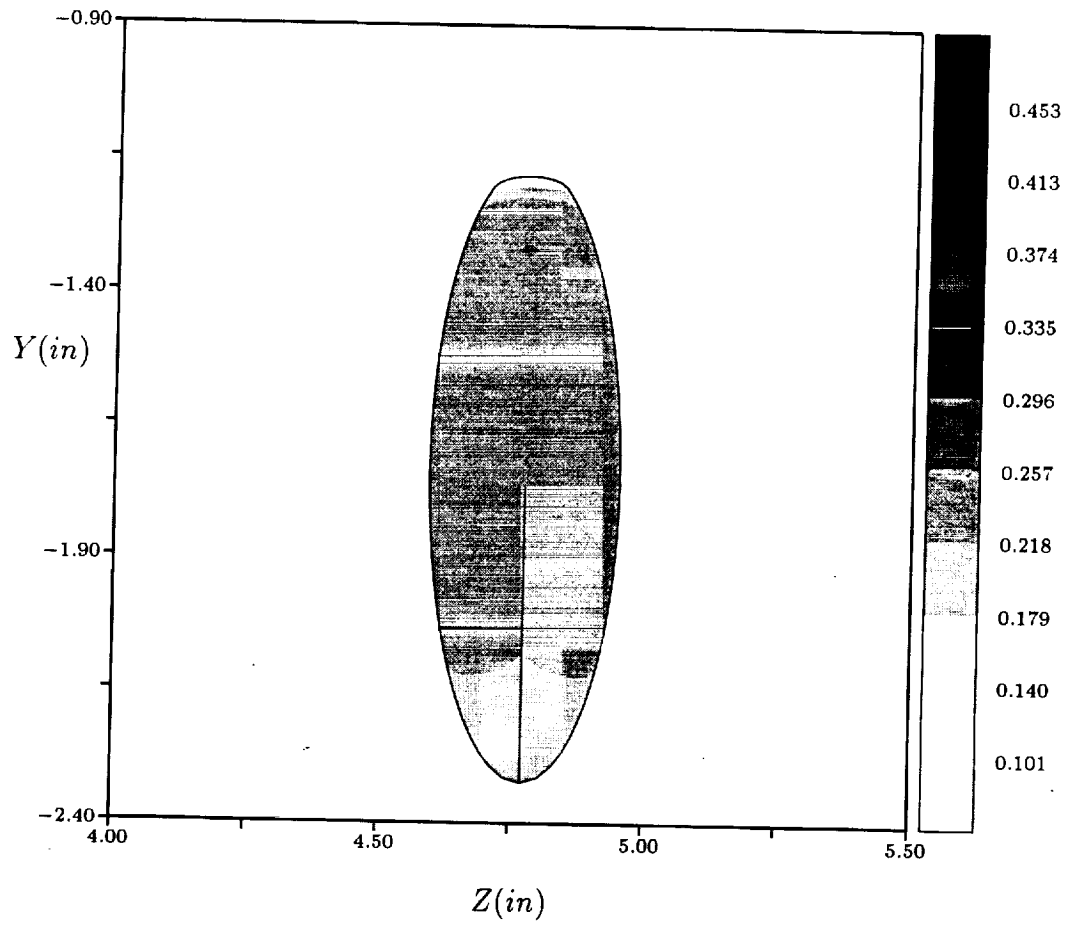
Figure 3: Mach contours in the inlet (i=1) plane of the FASTRAC turbine nozzle - RP1.

18
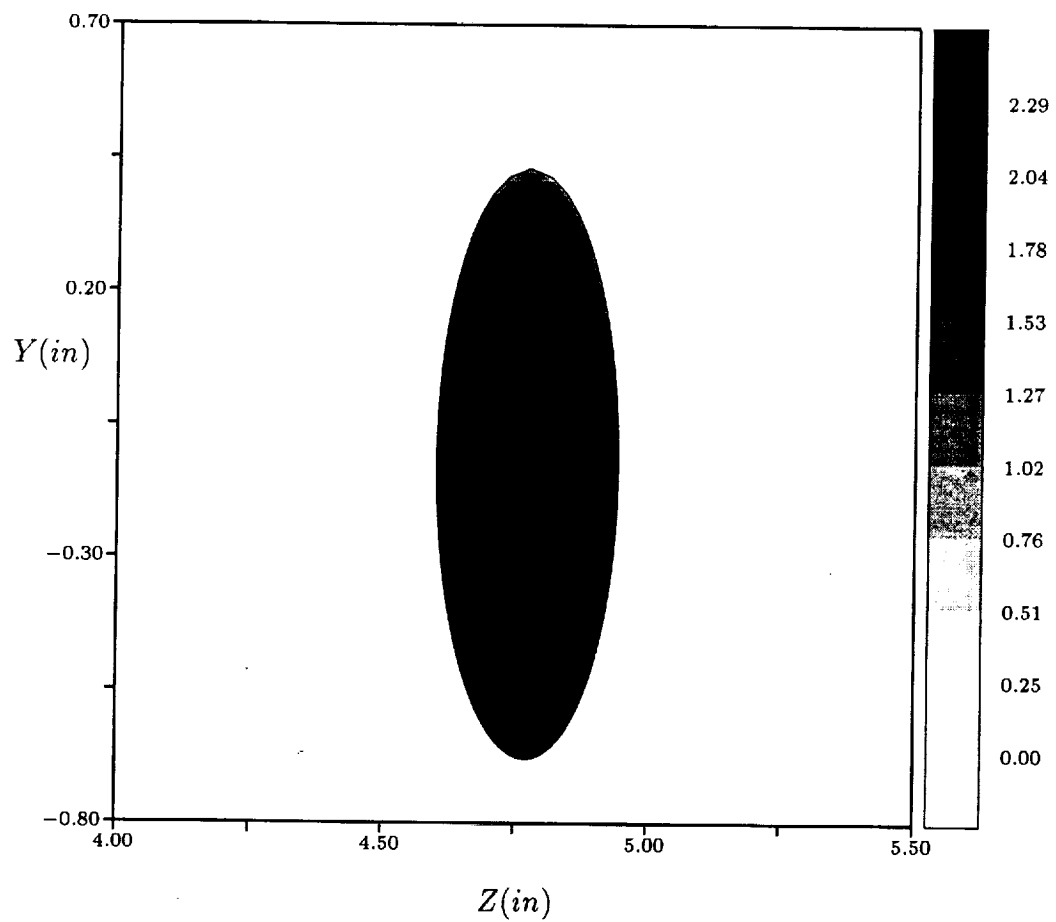
Figure 4: Mach contours in the exit (i=131) plane of the FASTRAC turbine nozzle - RP1.

19
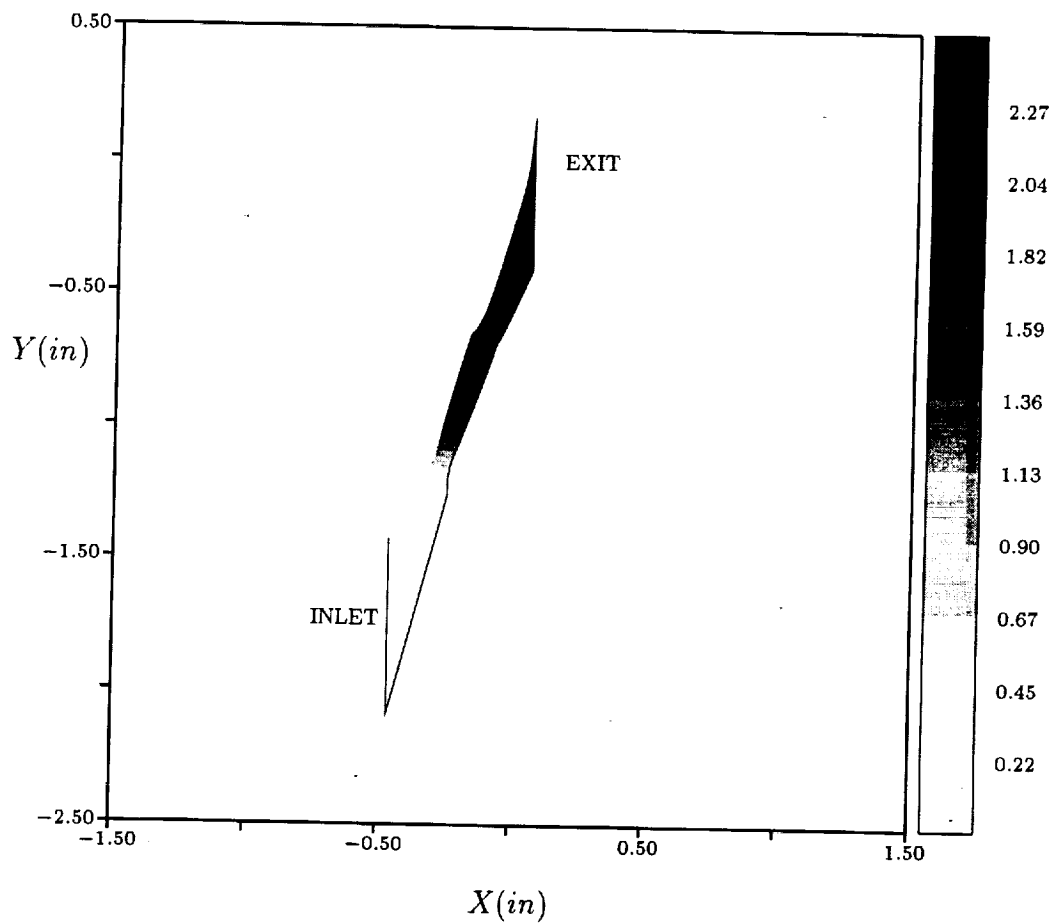
Figure 5: Mach contours in the k=4 plane of the FASTRAC turbine nozzle - RP1.
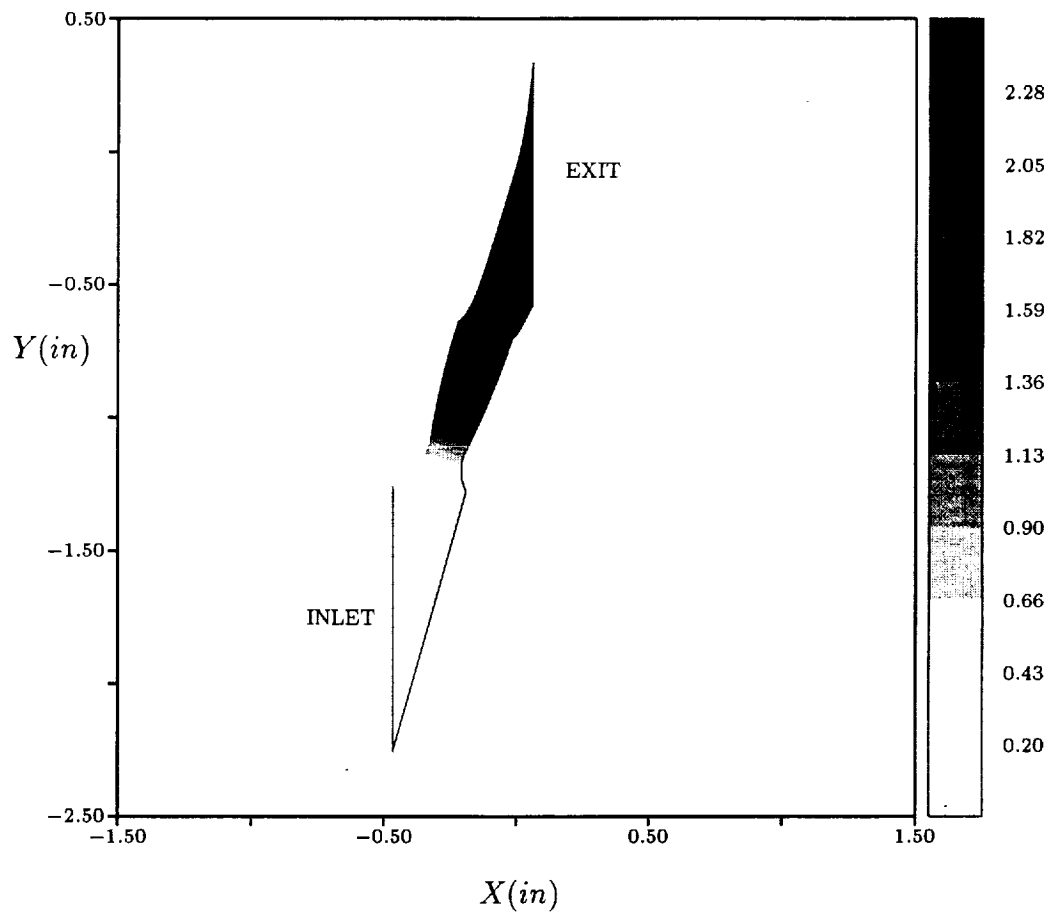
Figure 6: Mach contours in the k=8 plane of the FASTRAC turbine nozzle - RP1.
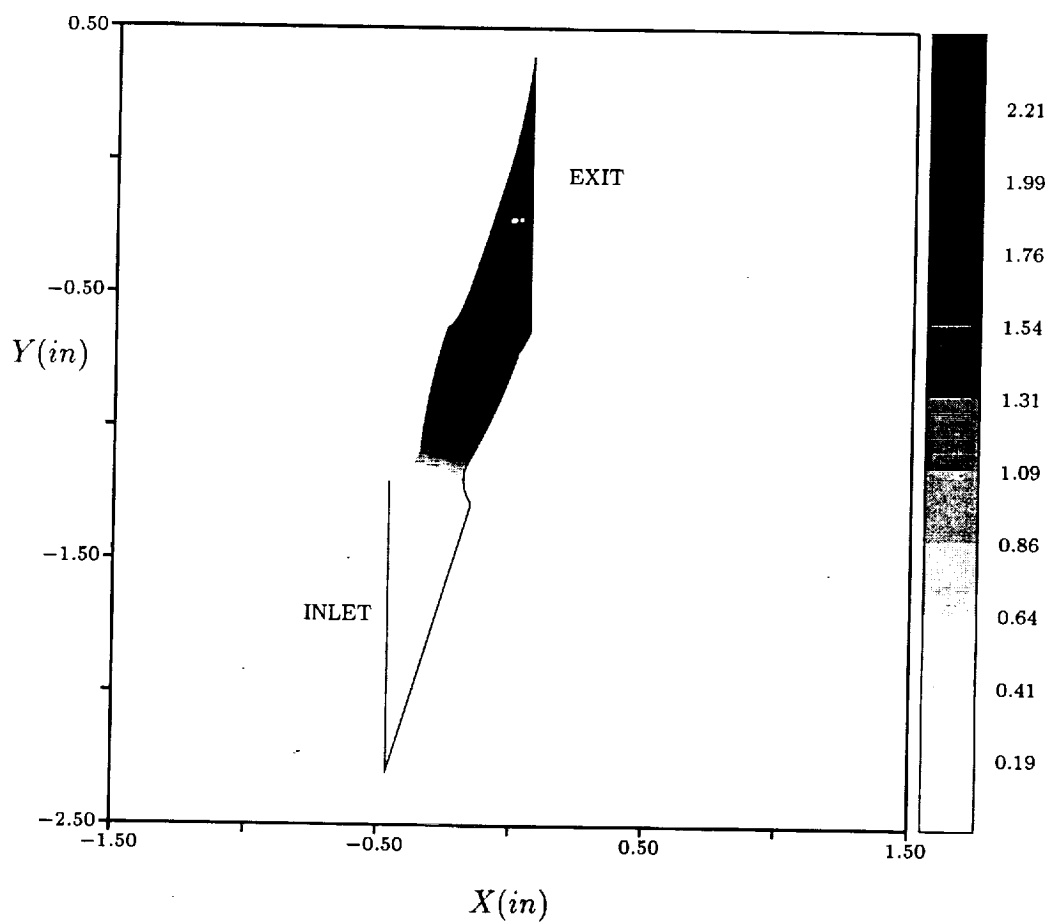
Figure 7: Mach contours in the k=12 plane of the FASTRAC turbine nozzle - RP1.
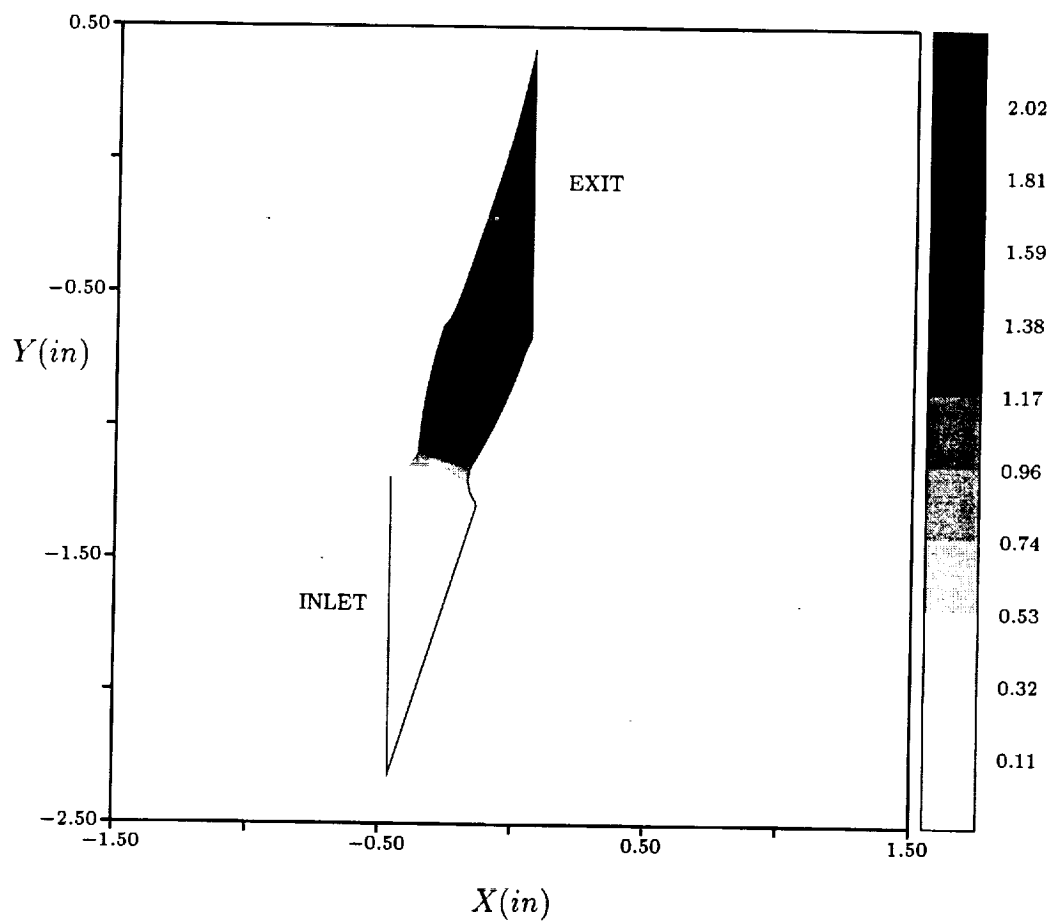
Figure 8: Mach contours in the k=16 plane of the FASTRAC turbine nozzle - RP1.
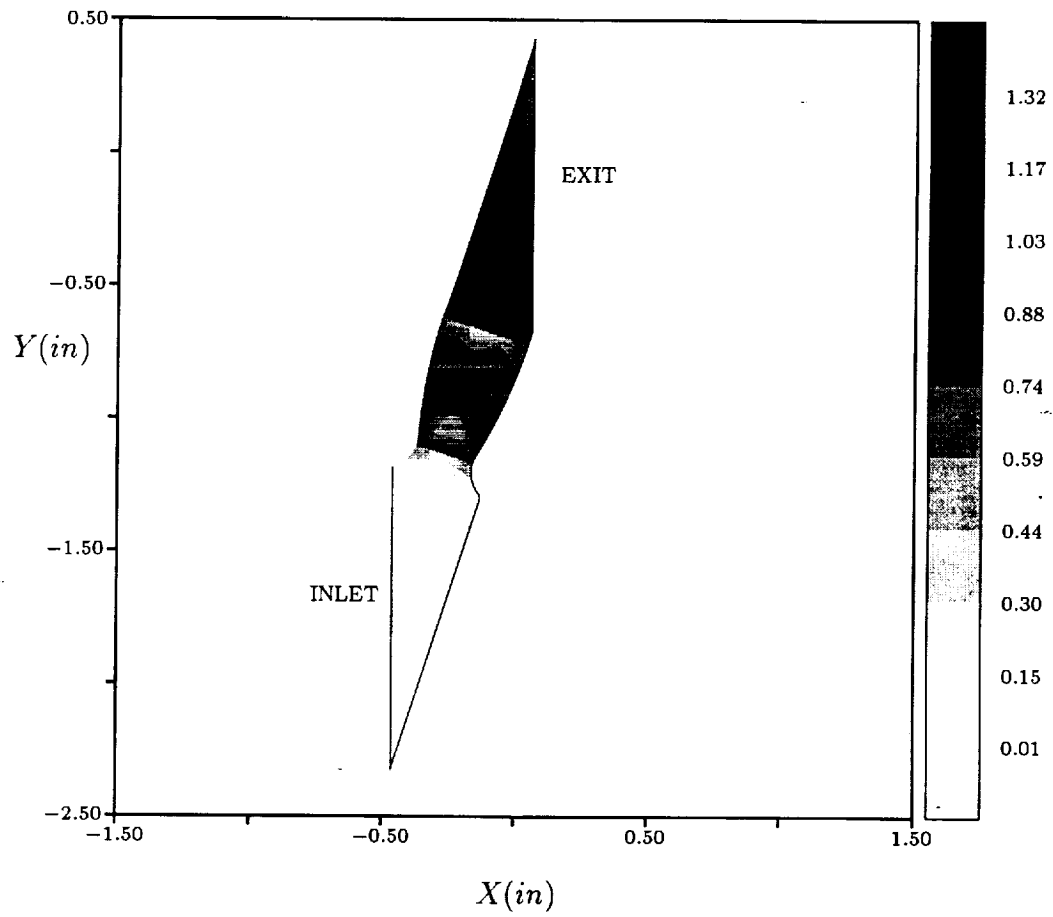
Figure 9: Mach contours in the k=20 plane of the FASTRAC turbine nozzle - RP1.
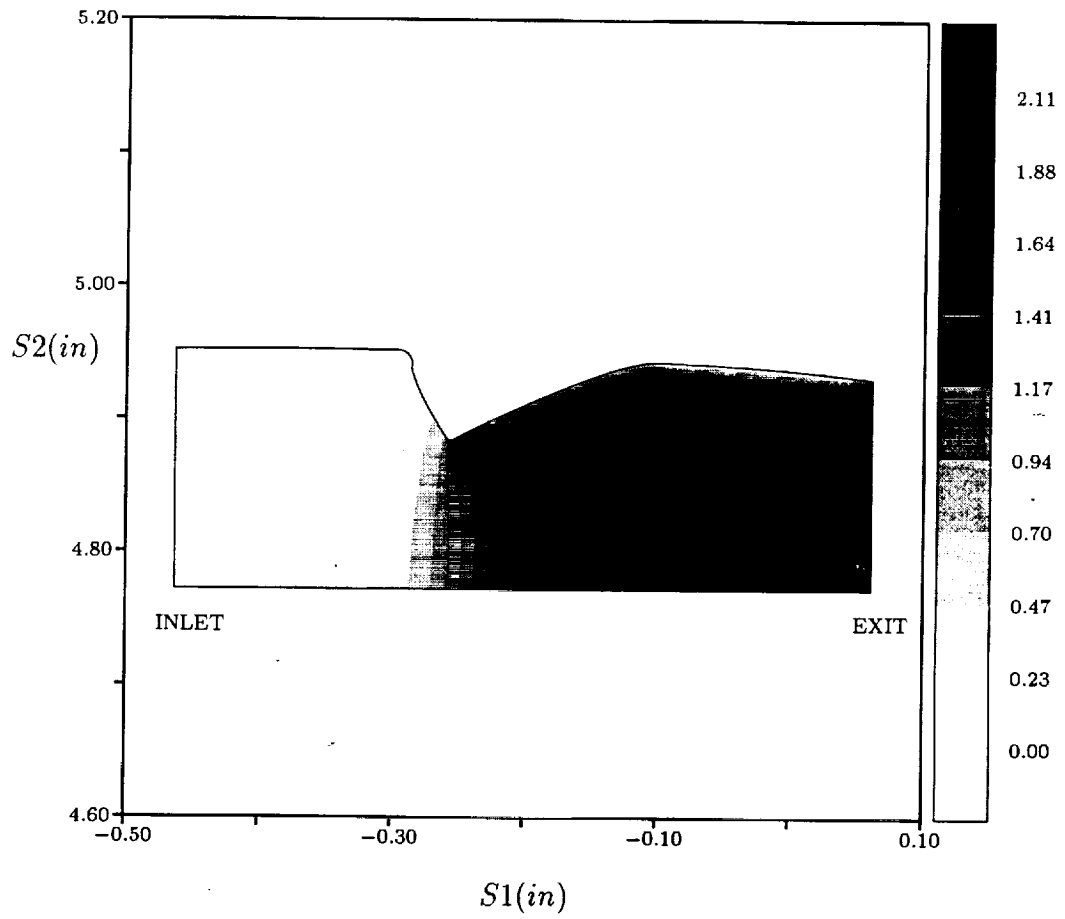
Figure 10: Mach contours in the j=20 plane of the FASTRAC turbine nozzle - RP1.
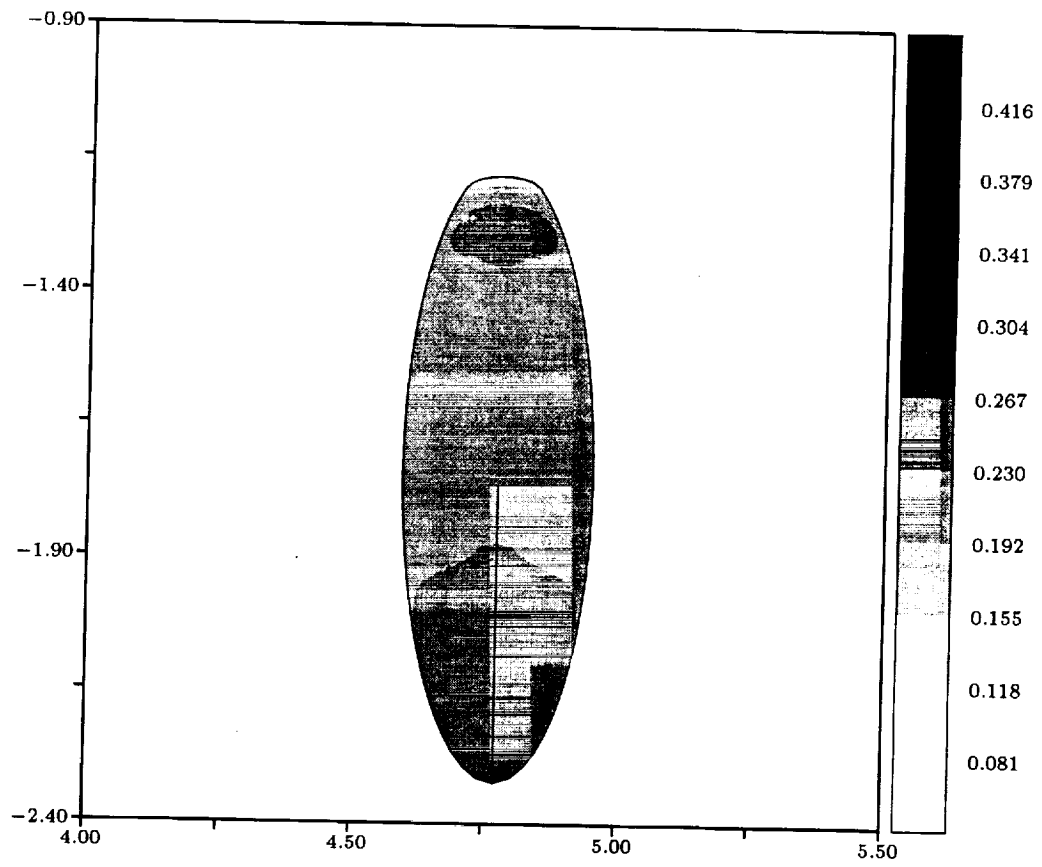
Figure 11: Mach contours in the inlet (i=1) plane of the FASTRAC turbine nozzle - N_2.
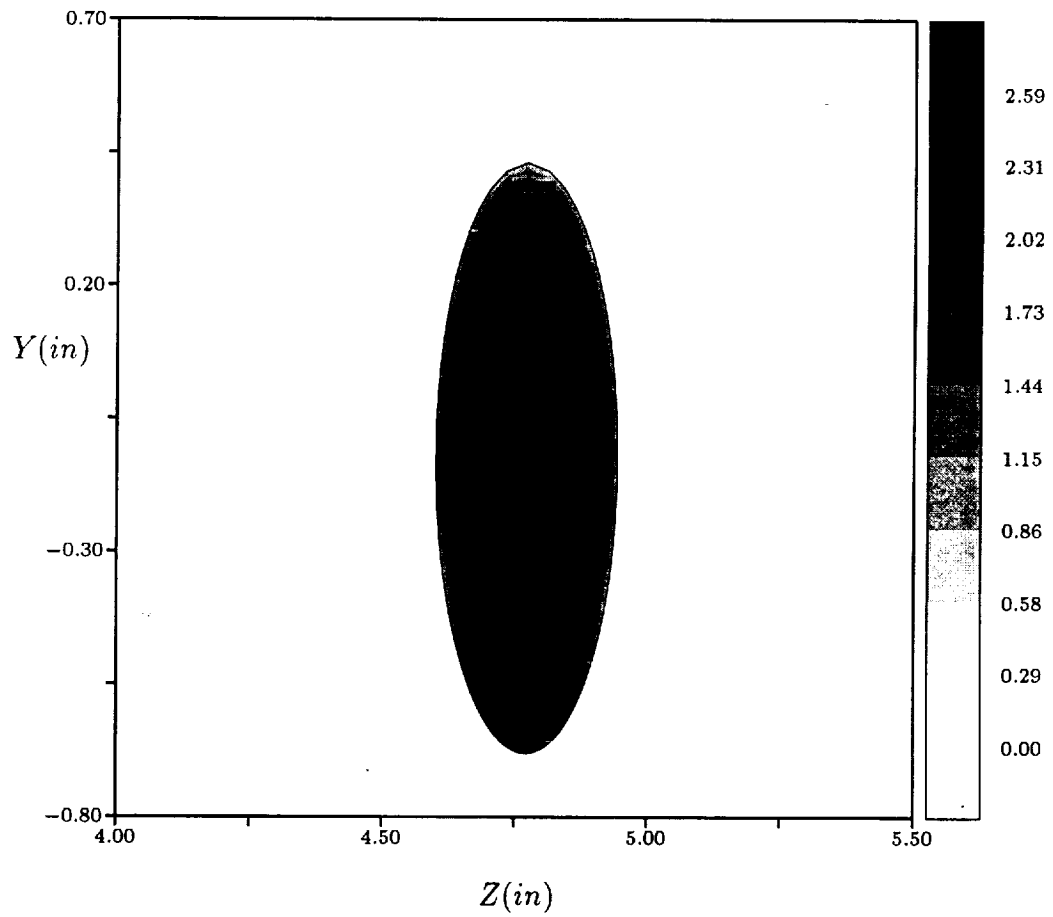
Figure 12: Mach contours in the exit (i=131) plane of the FASTRAC turbine nozzle - N_2.
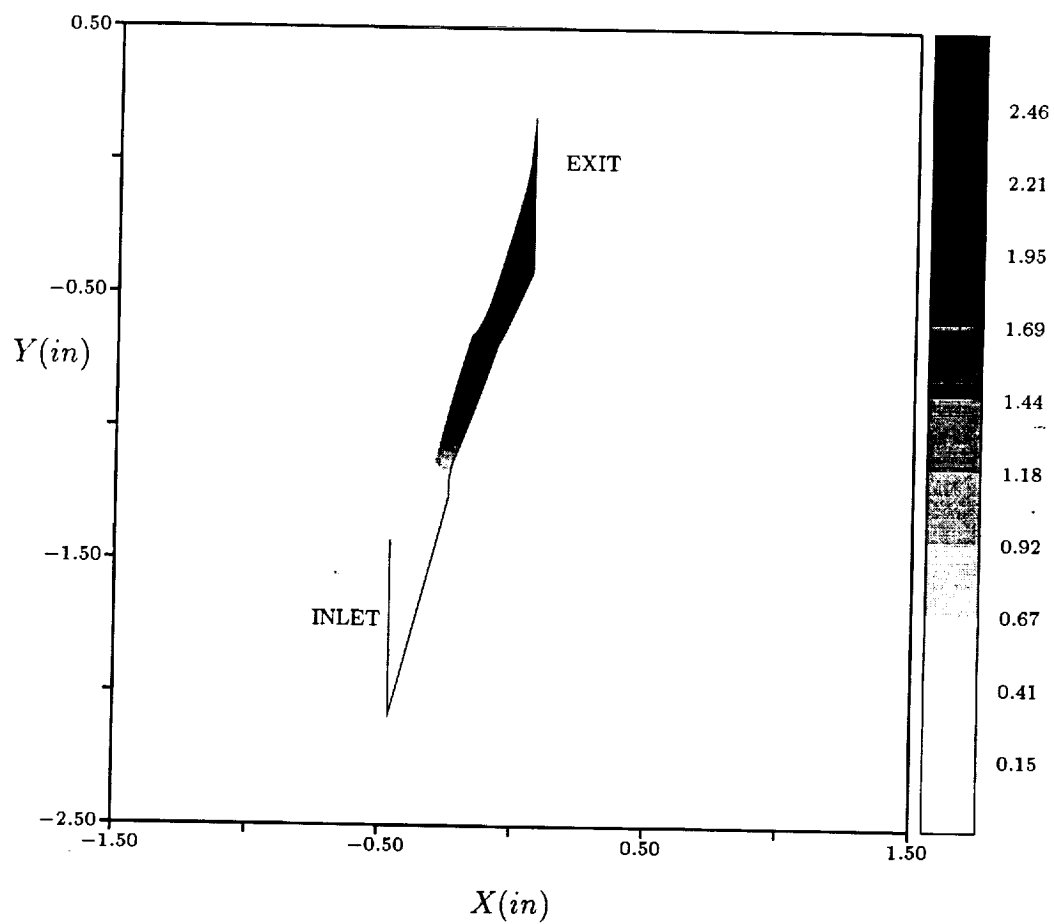
Figure 13: Mach contours in the k=4 plane of the FASTRAC turbine nozzle - N_2.

0.50

2.53

2.26

EXIT

2.00

−0.50

1.73

$Y(in)$

1.47

1.20

0.94

−1.50

0.68

INLET

0.41

0.15

−2.50
−1.50   −0.50   0.50   1.50

$X(in)$
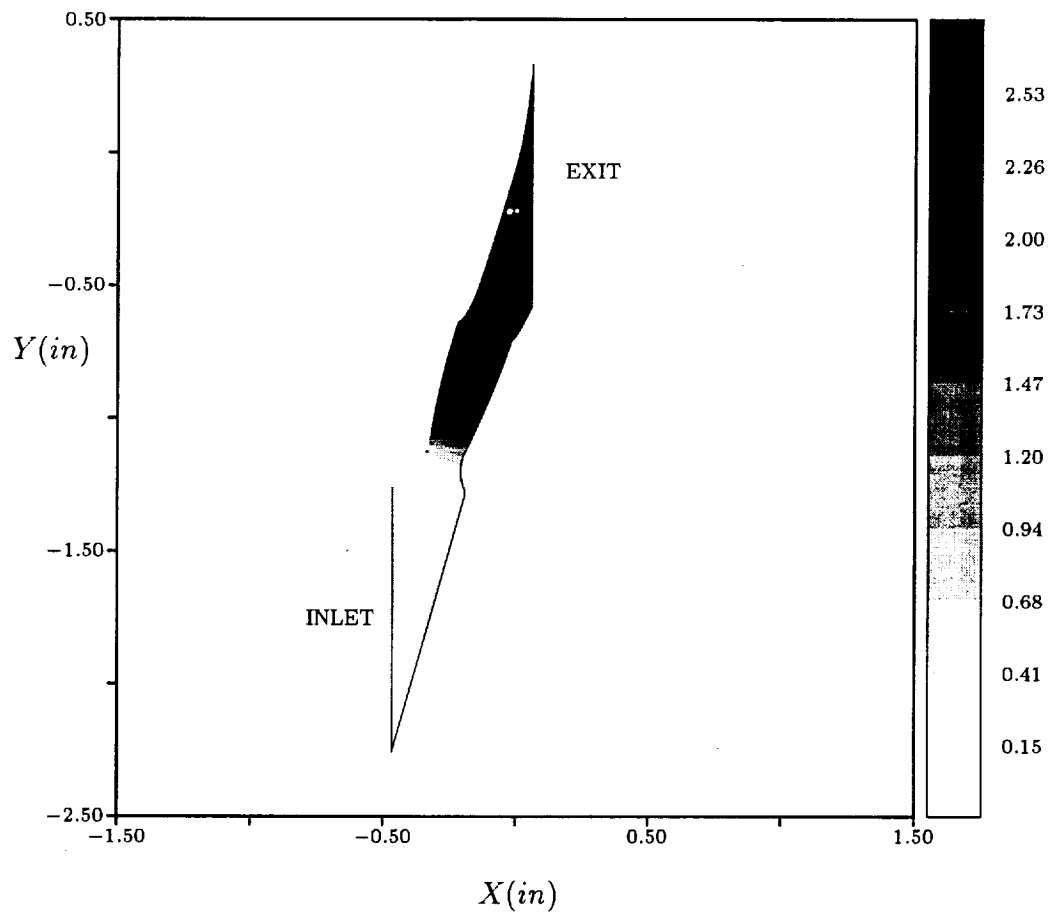
Figure 14: Mach contours in the k=8 plane of the FASTRAC turbine nozzle - N_2.
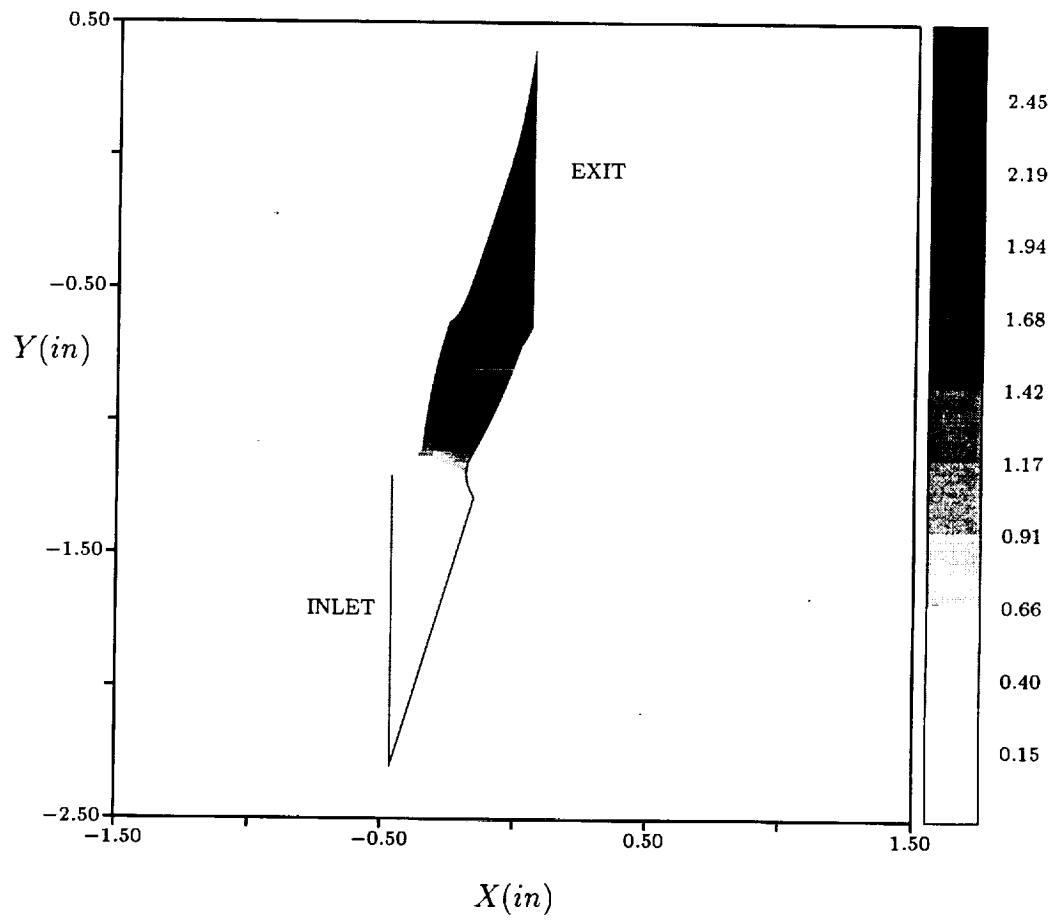
Figure 15: Mach contours in the k=12 plane of the FASTRAC turbine nozzle - N_2.
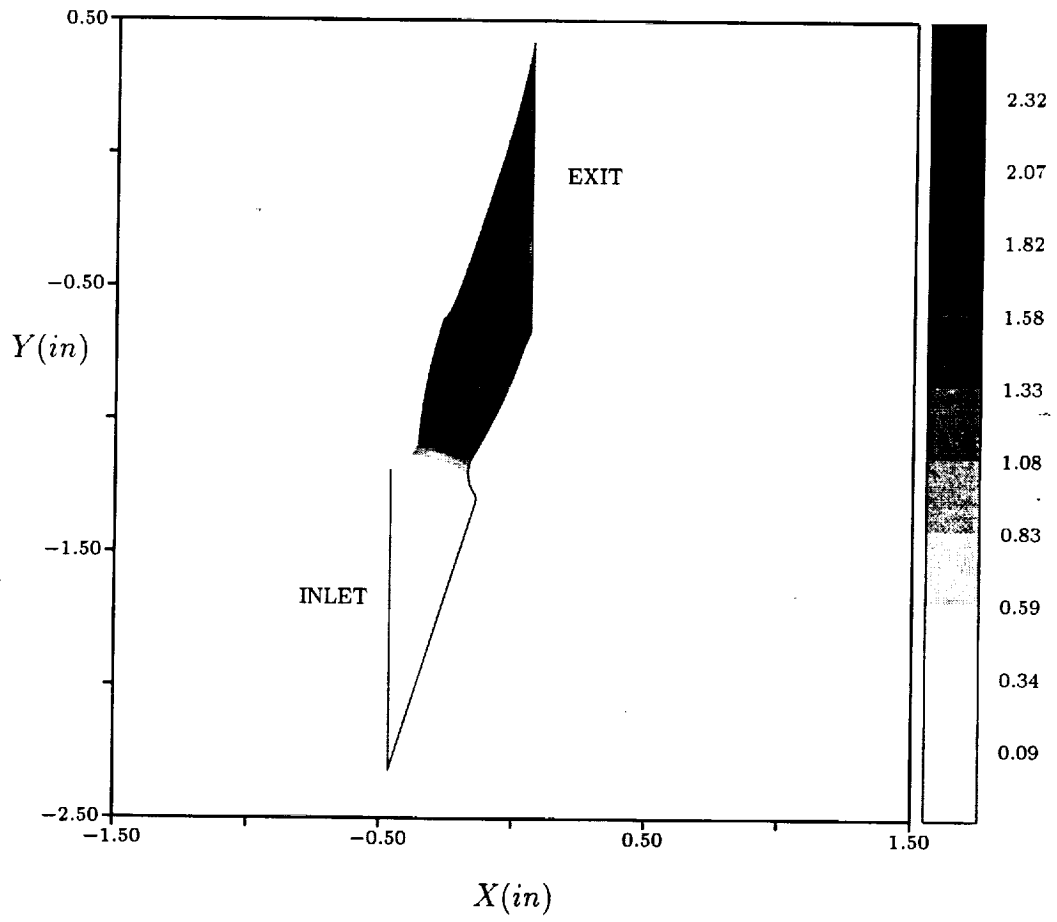
Figure 16: Mach contours in the k=16 plane of the FASTRAC turbine nozzle - N_2.
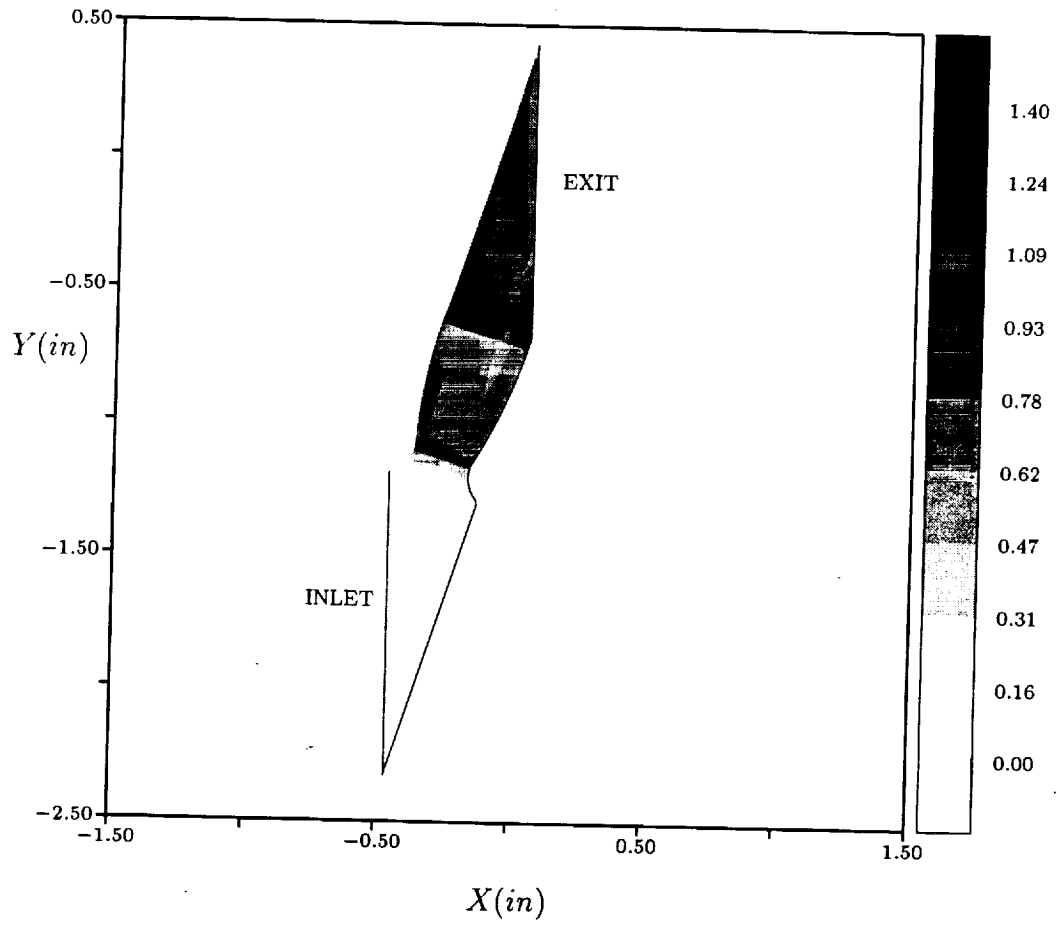
Figure 17: Mach contours in the k=20 plane of the FASTRAC turbine nozzle - N_2.
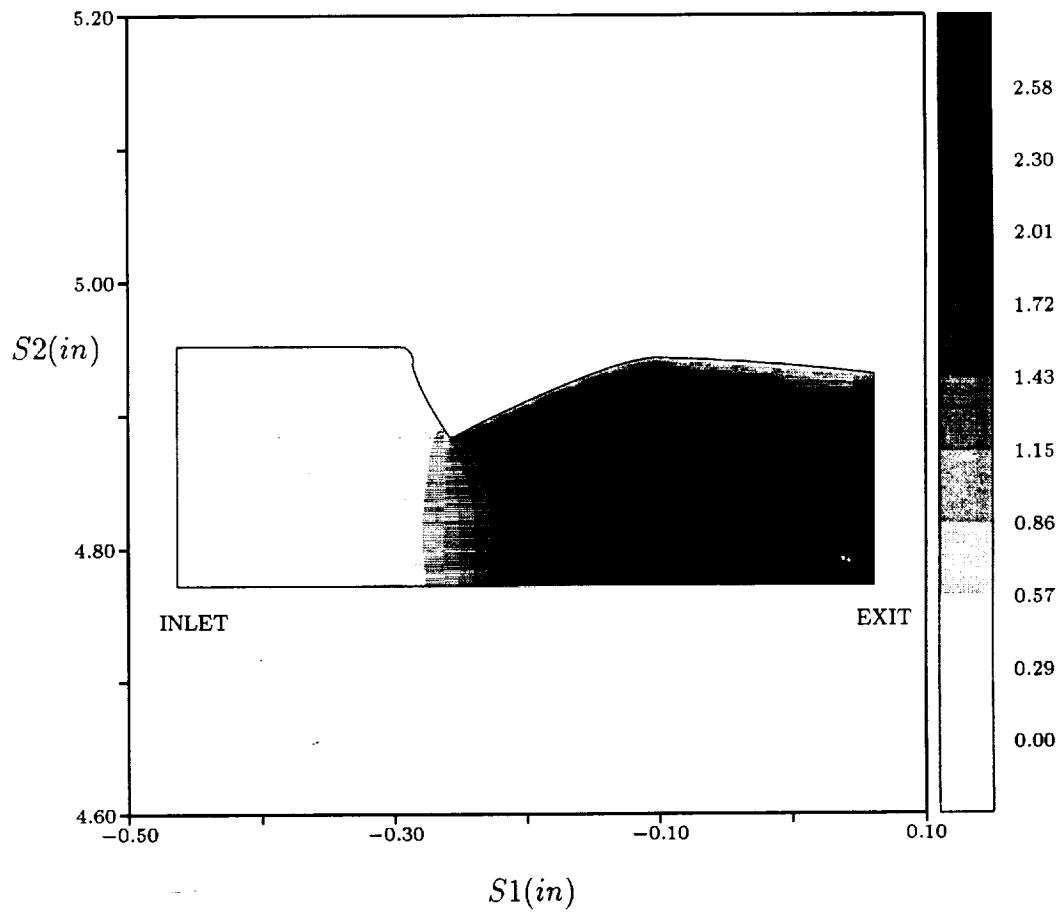
Figure 18: Mach contours in the j=20 plane of the FASTRAC turbine nozzle - N_2.
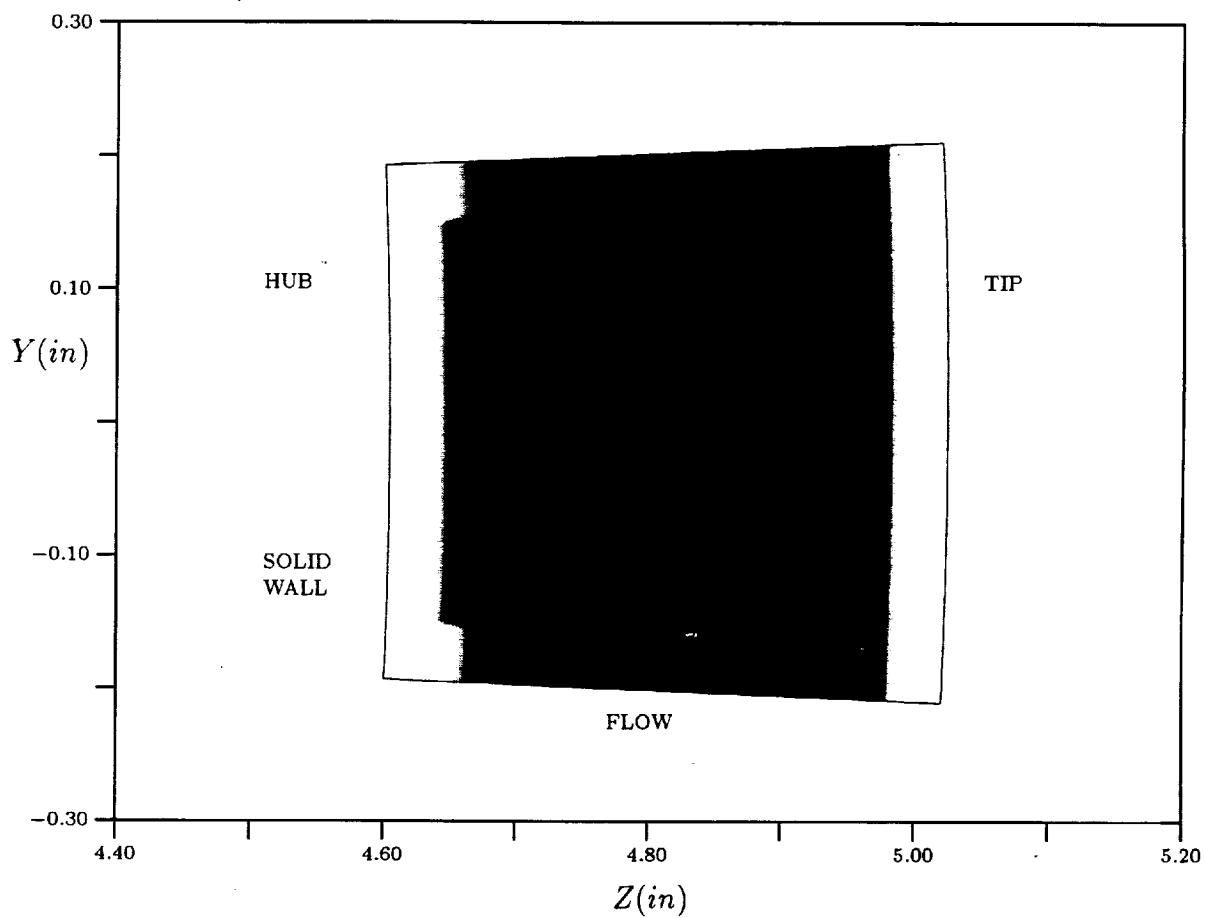
Figure 19: Inlet nozzle definition.
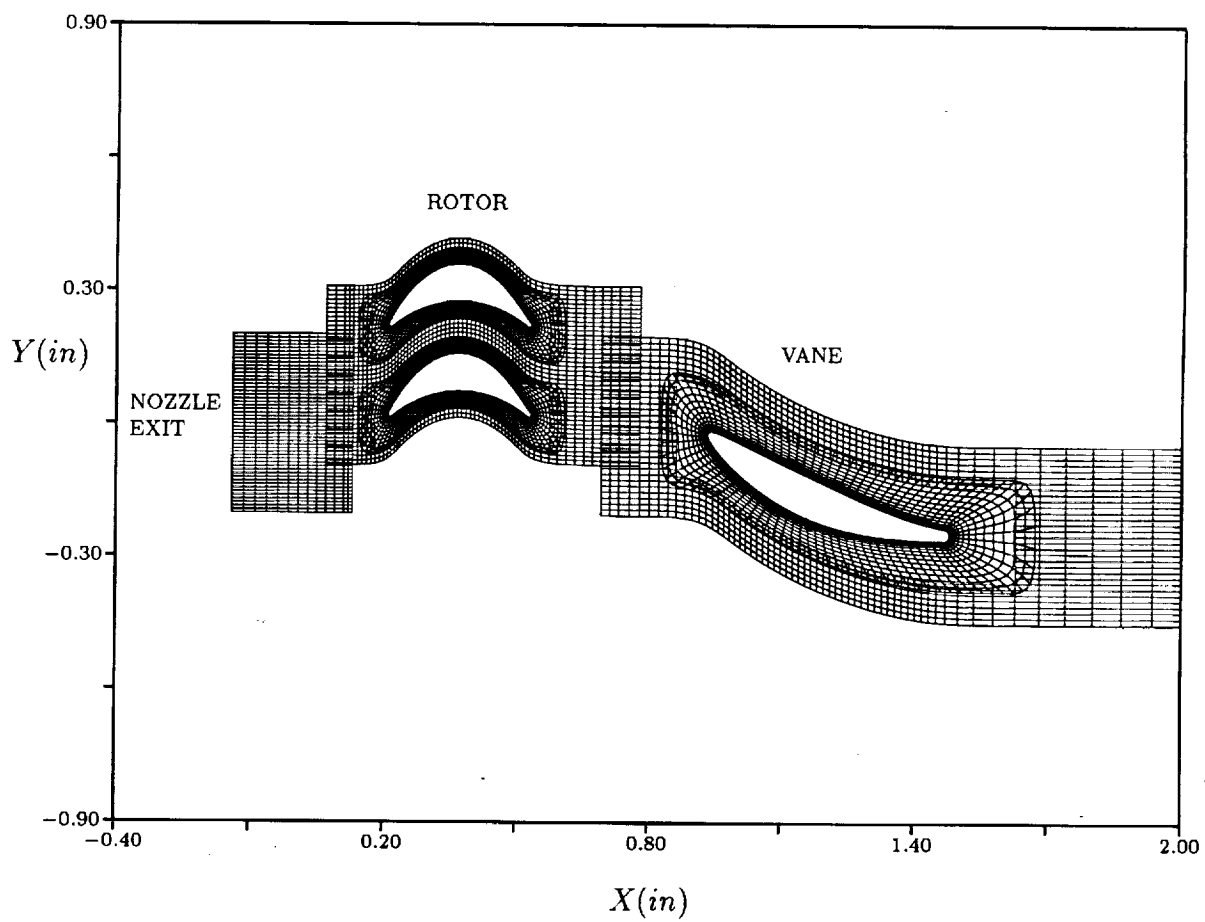
Figure 20: Grid topology for FASTRAC turbine (x-y).
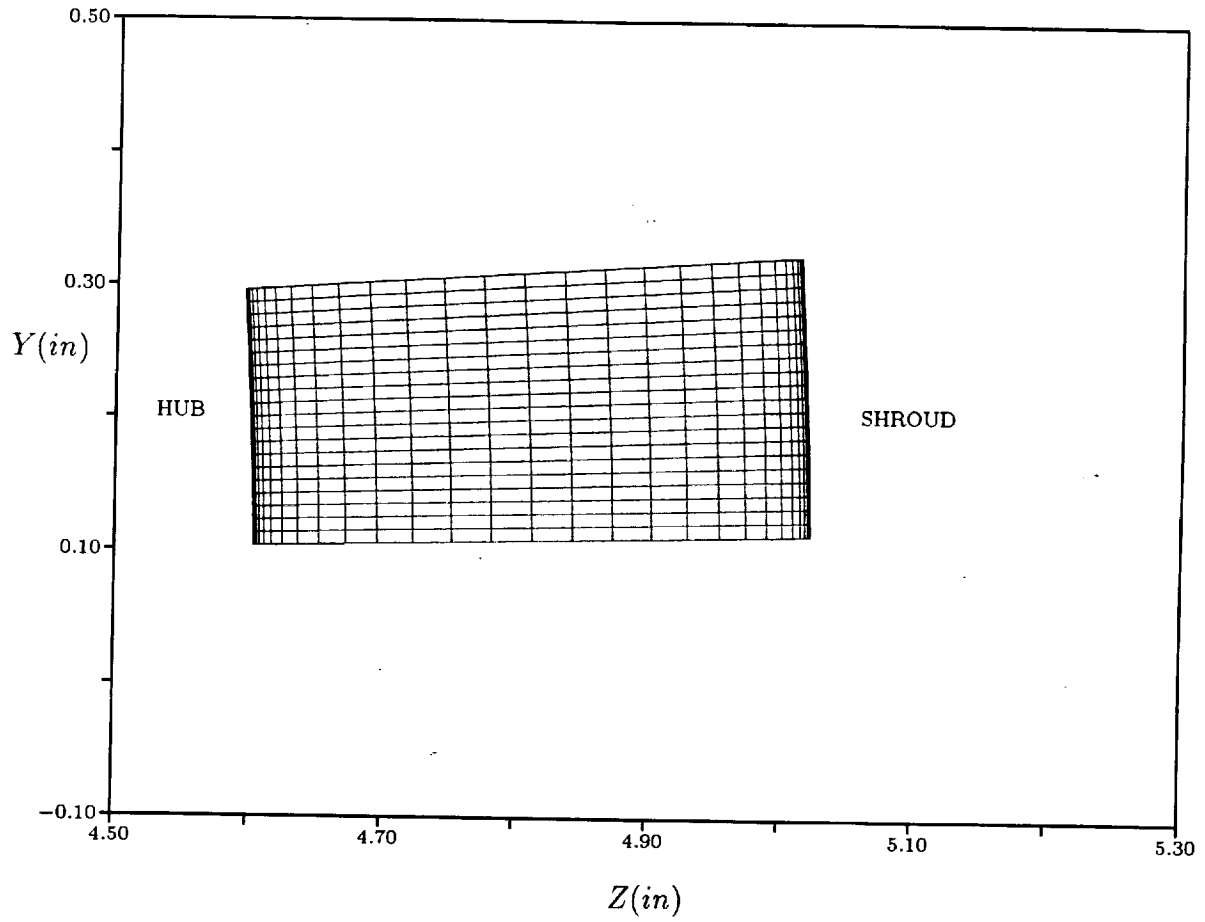
Figure 21: Grid topology for FASTRAC turbine (z-y).
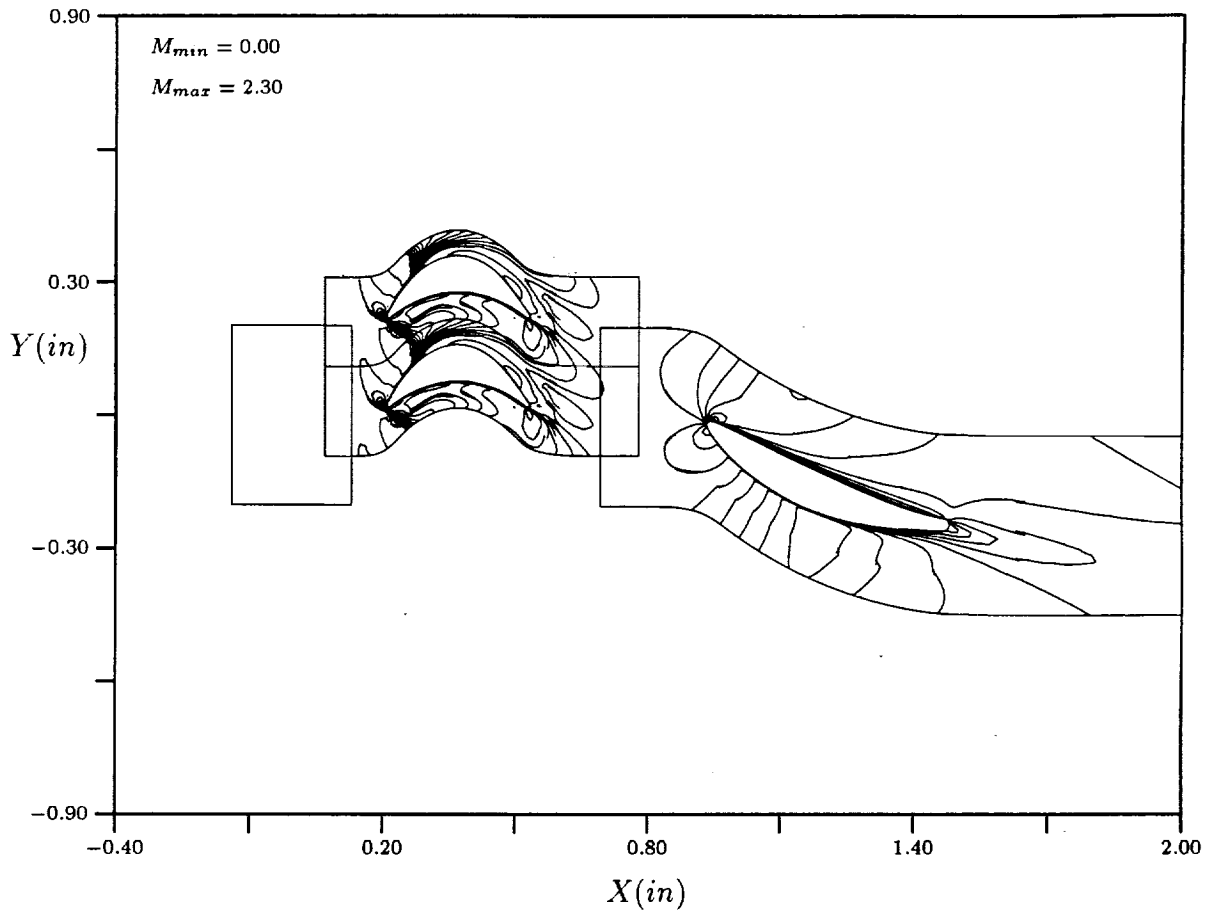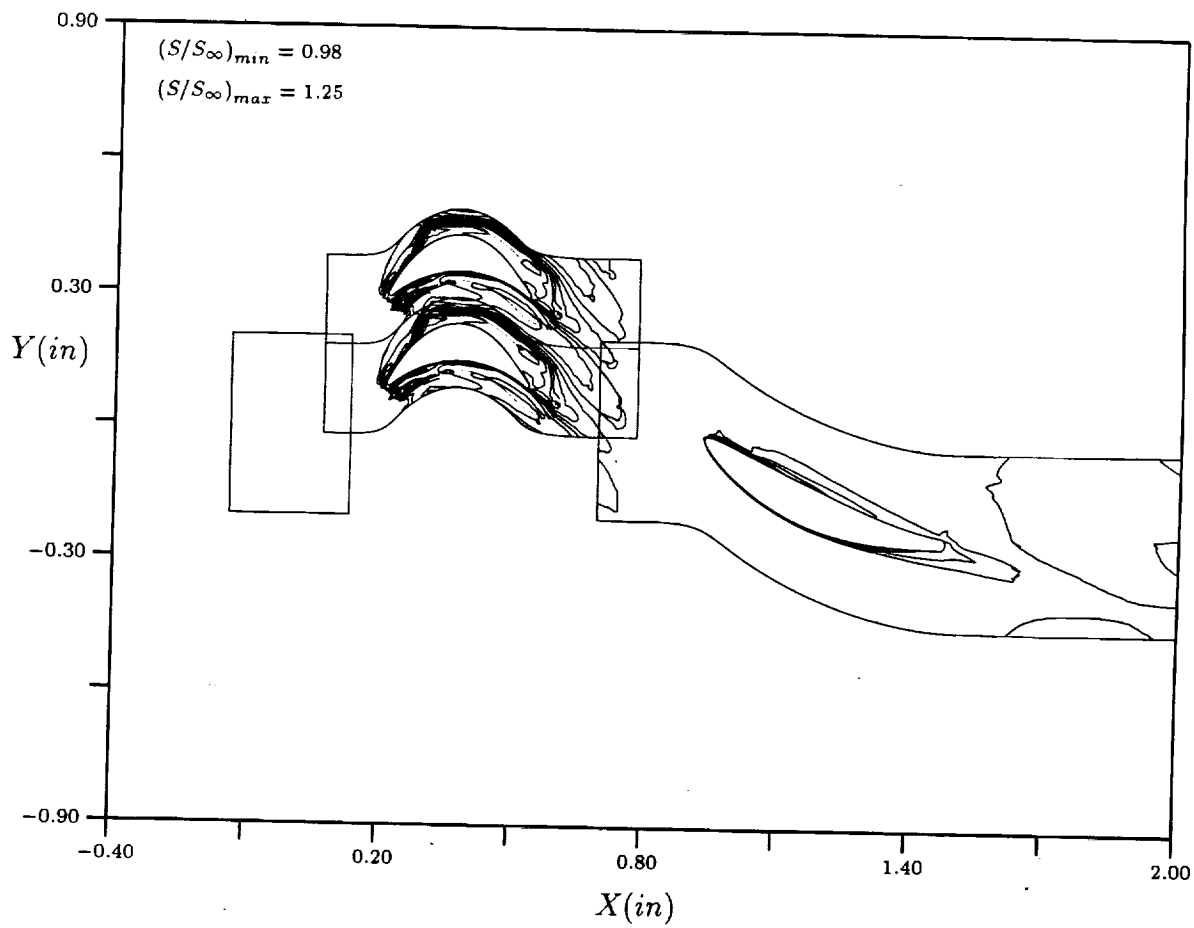
Figure 22: Mach contours at midspan - 0% cycle.
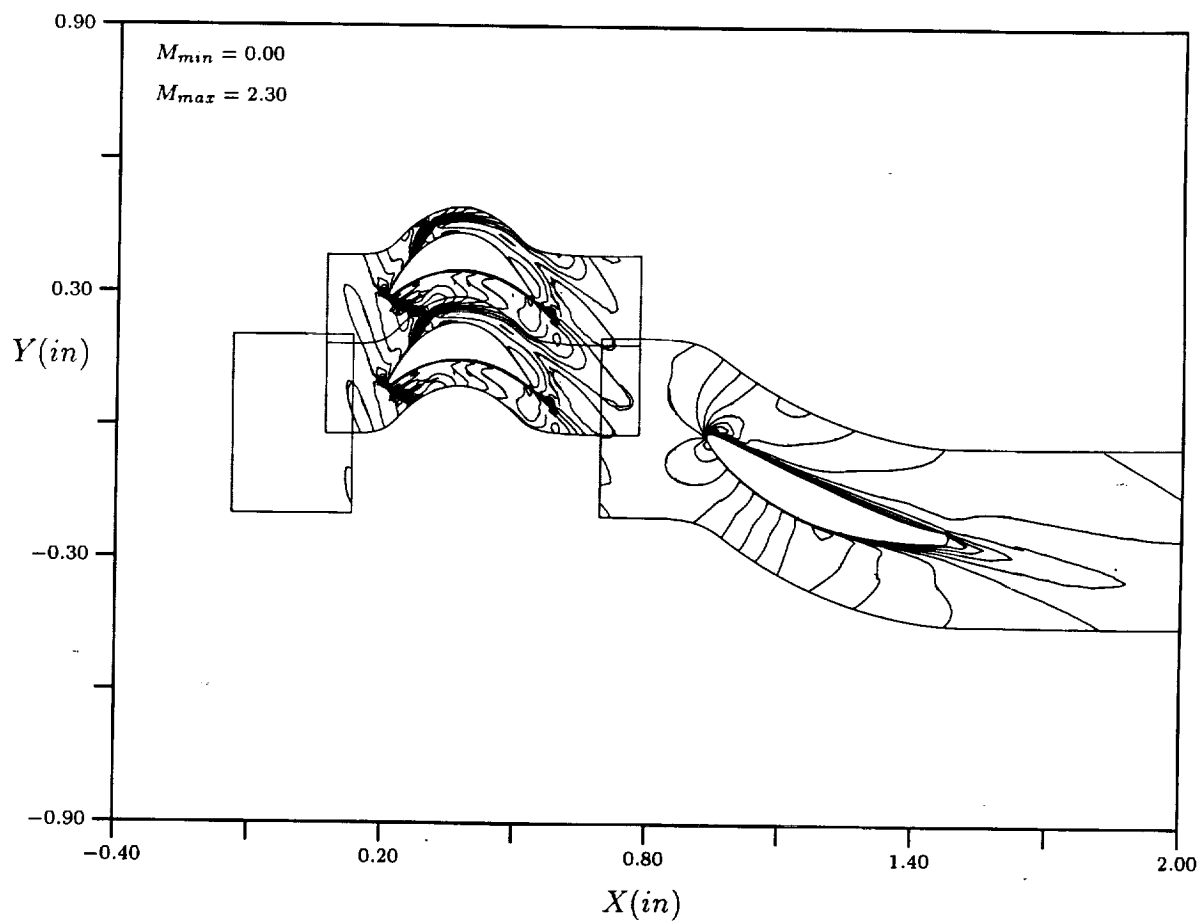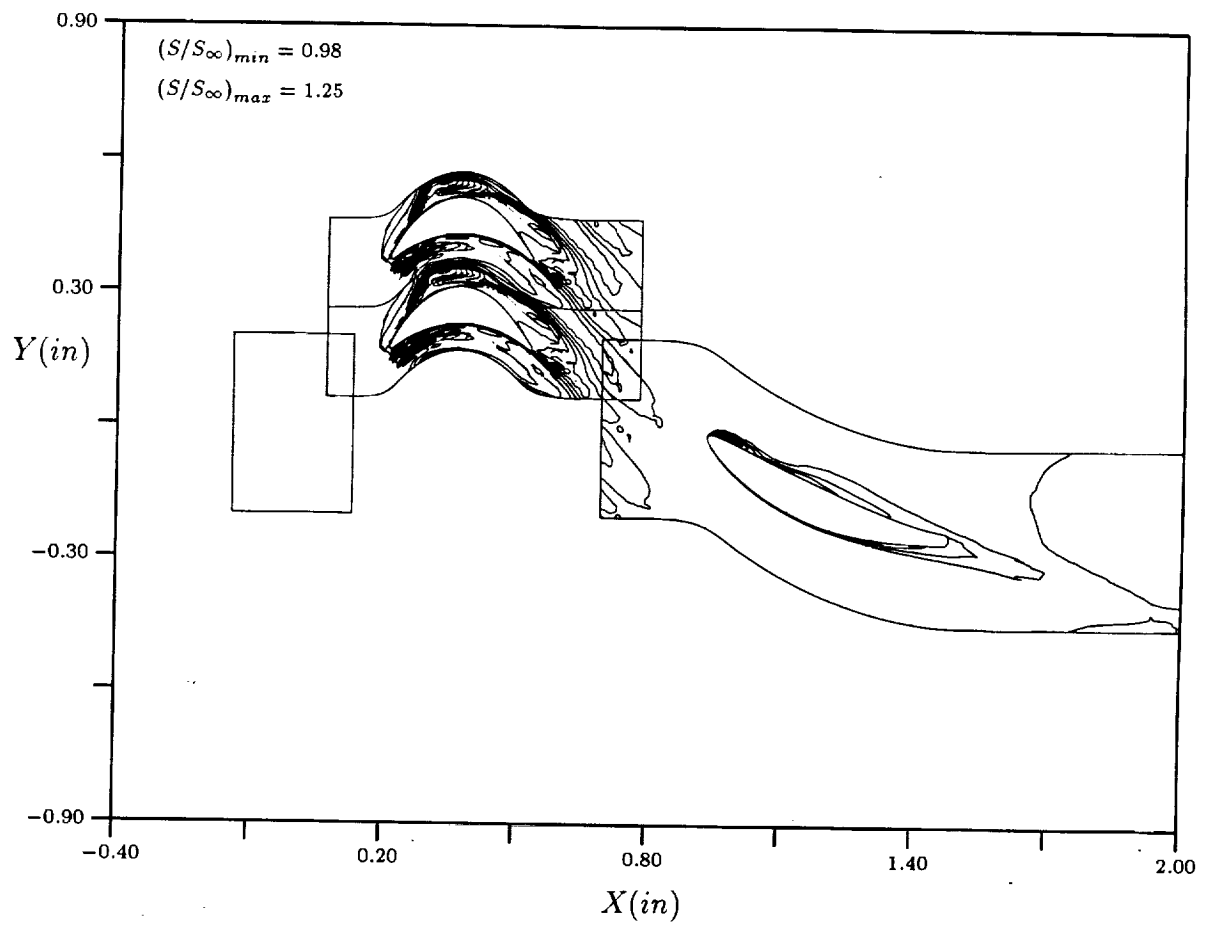
Figure 23: Mach contours at midspan - 20% cycle.
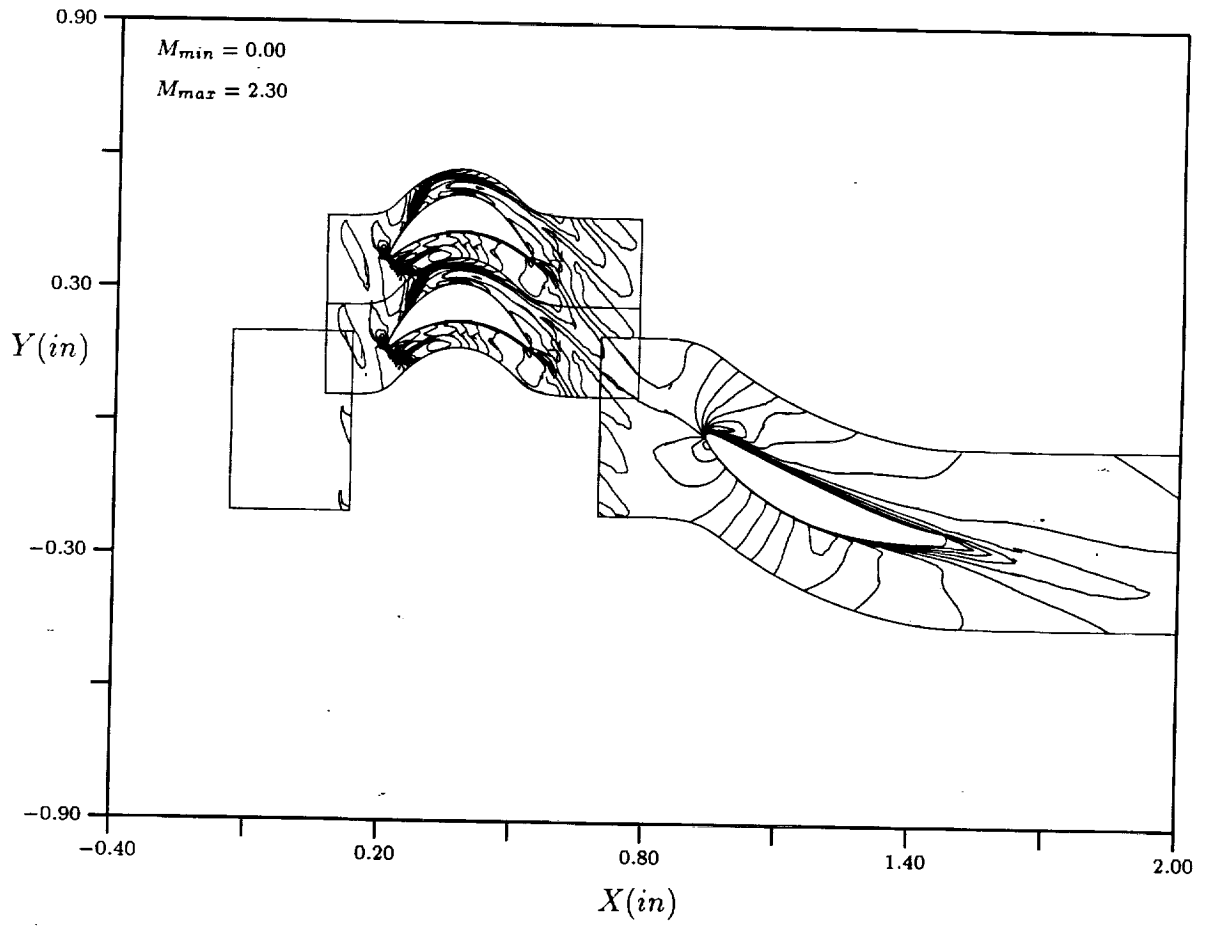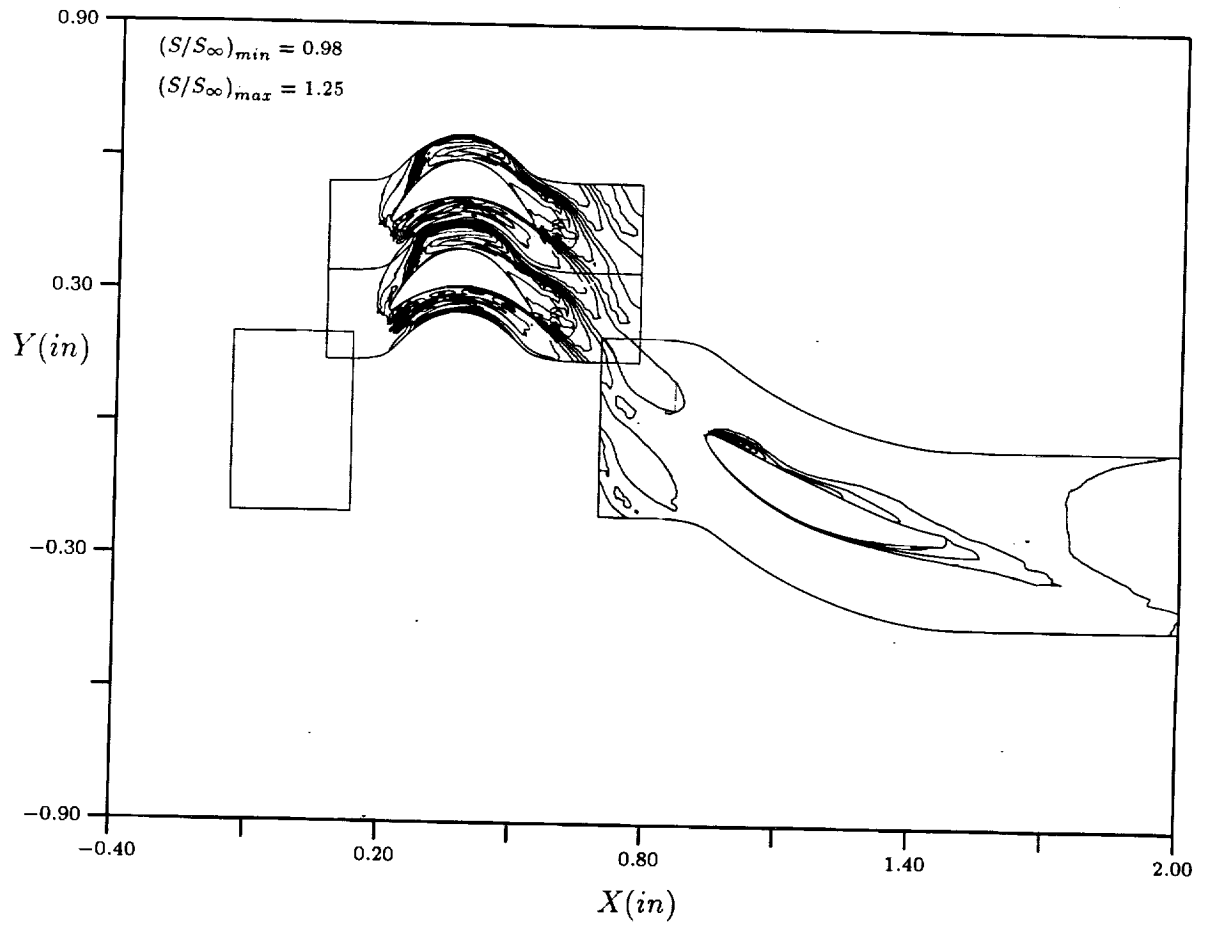
Figure 24: Mach contours at midspan - 40% cycle.
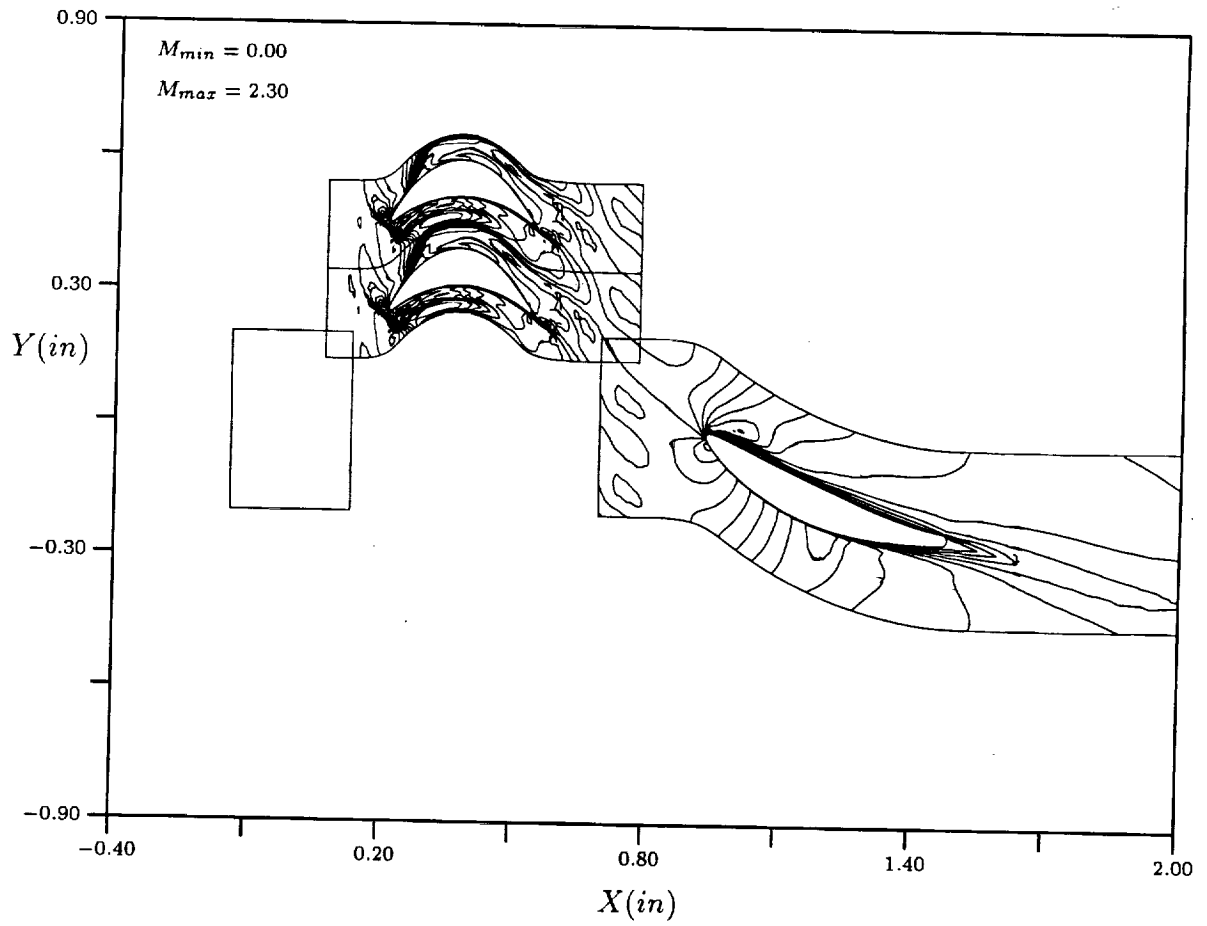
Figure 25: Mach contours at midspan - 60% cycle.

40
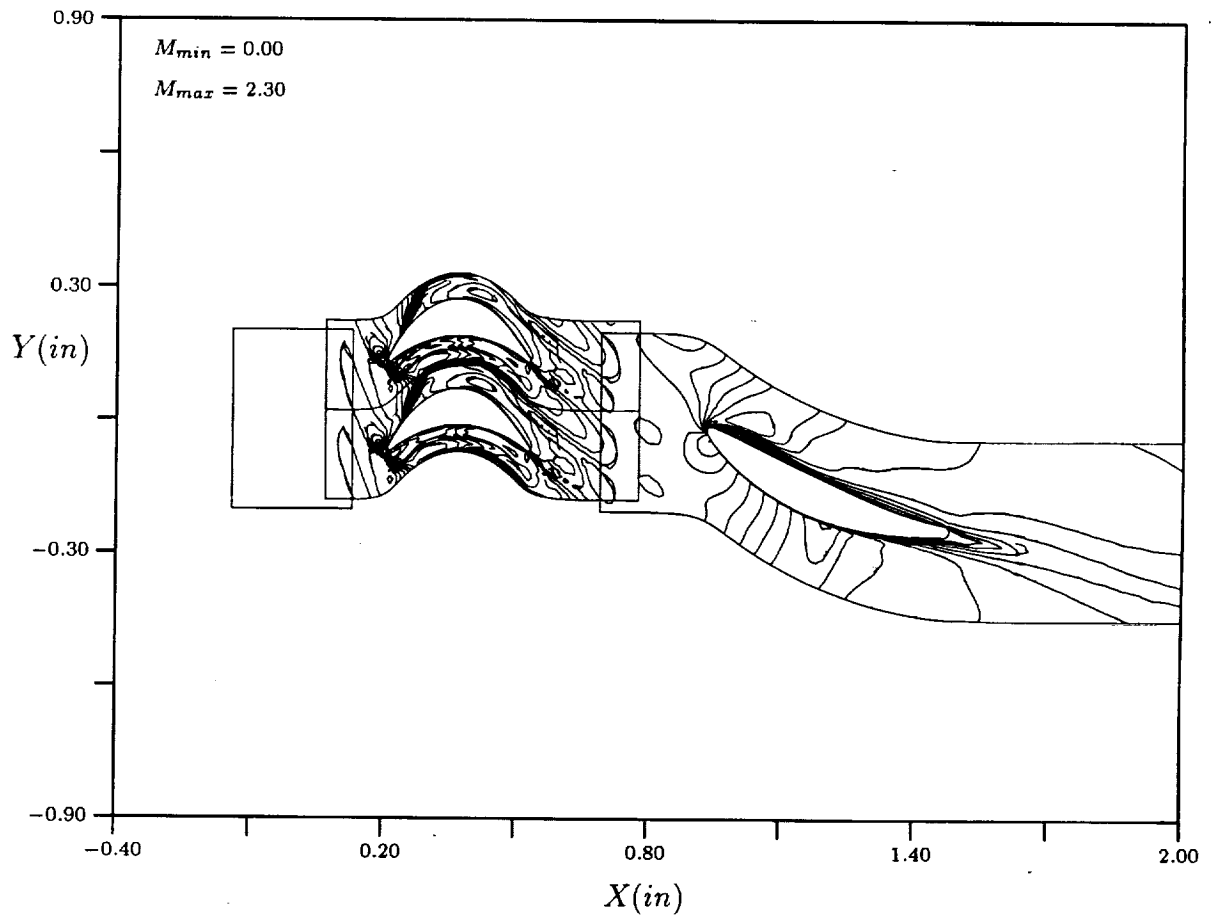
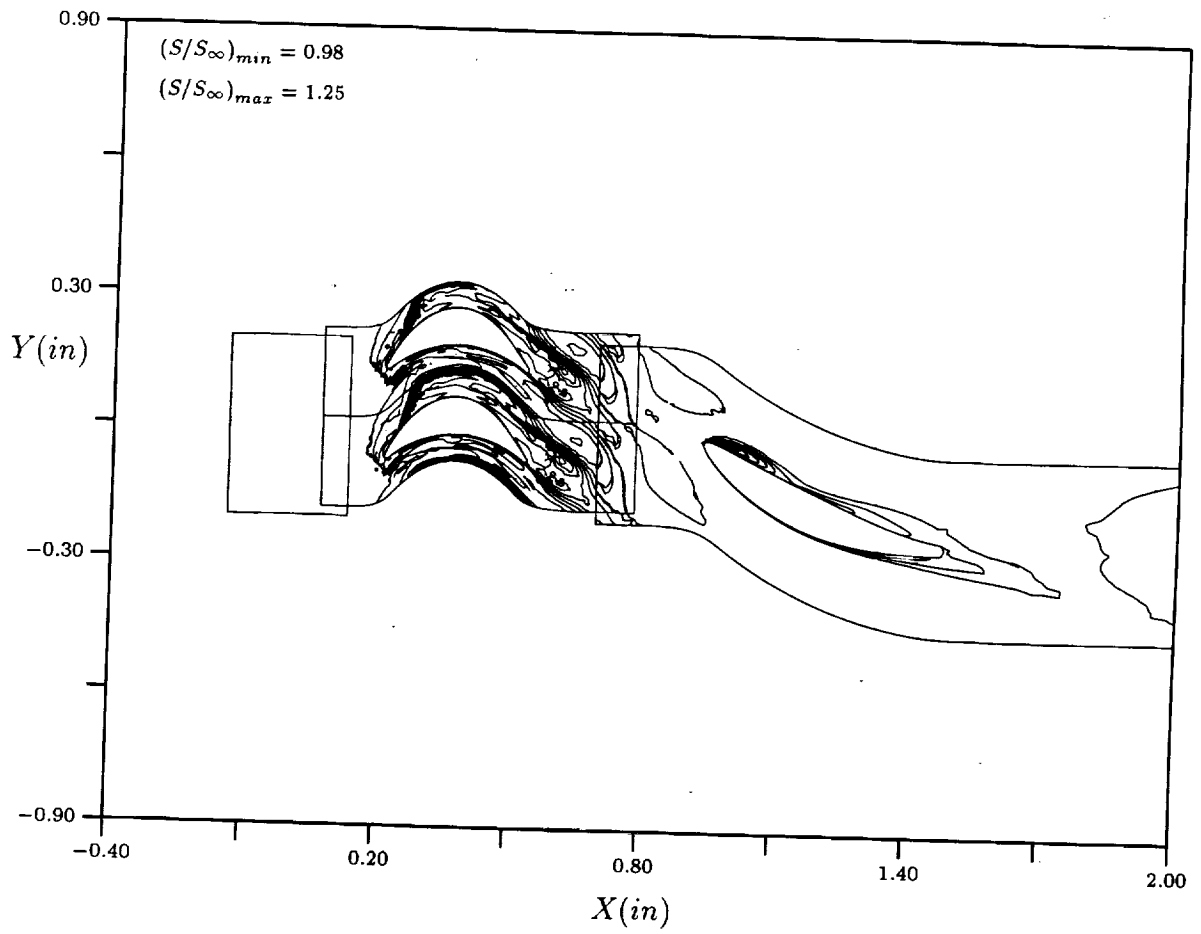Figure 26: Mach contours at midspan - 80% cycle.
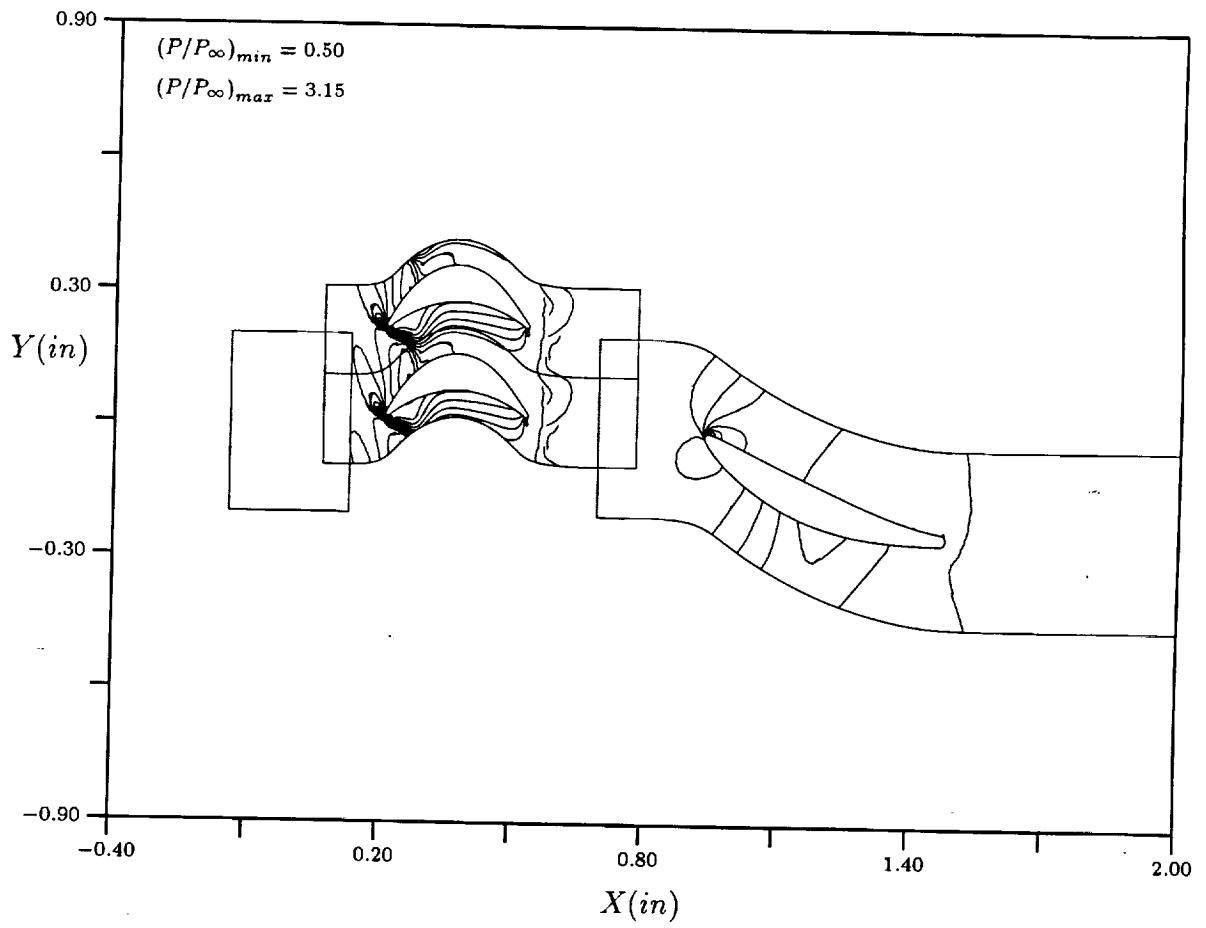
Figure 27: Static pressure contours at midspan - 0% cycle.
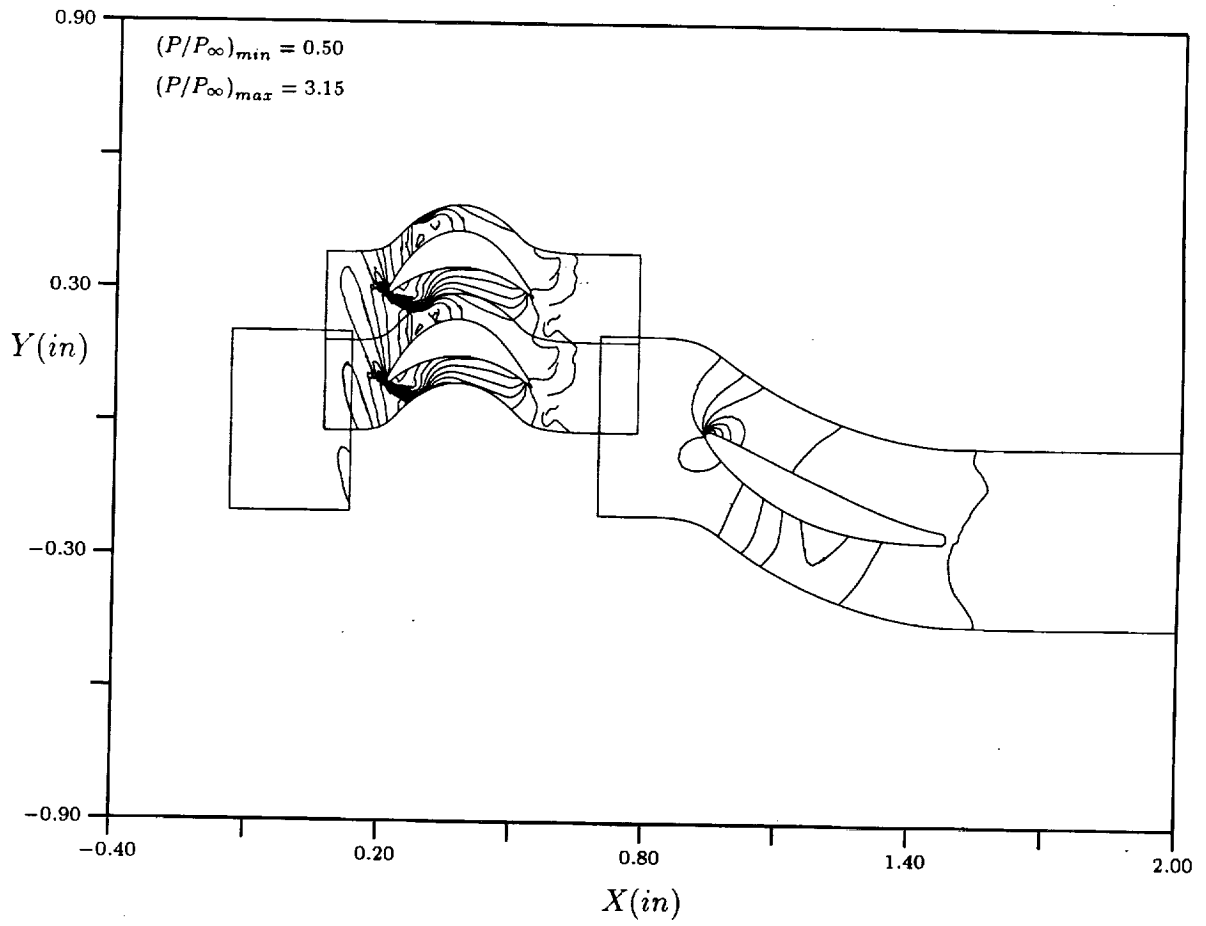
Figure 28: Static pressure contours at midspan - 20% cycle.

$(P/P_\infty)_{min} = 0.50$

$(P/P_\infty)_{max} = 3.15$
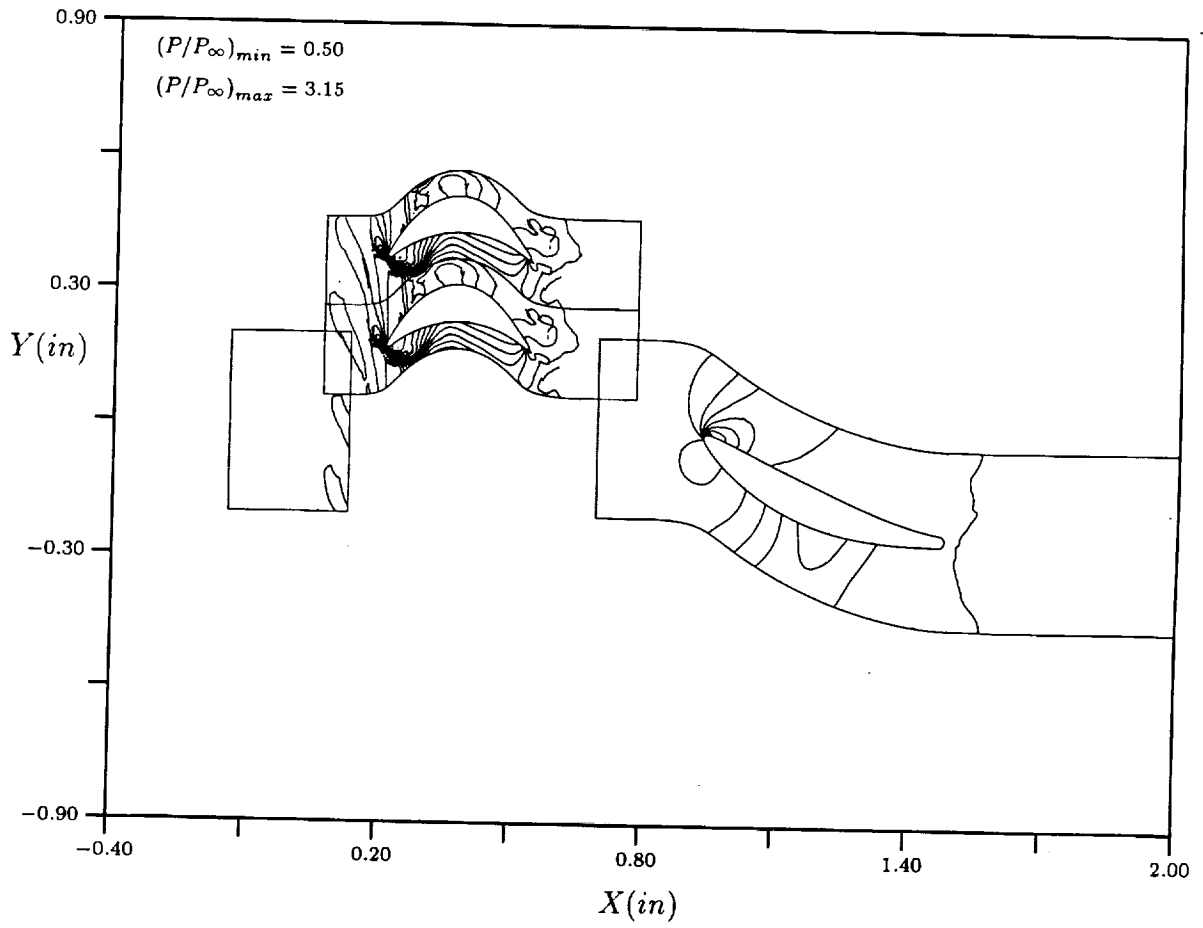
Figure 29: Static pressure contours at midspan - 40% cycle.

$(P/P_\infty)_{min} = 0.50$

$(P/P_\infty)_{max} = 3.15$
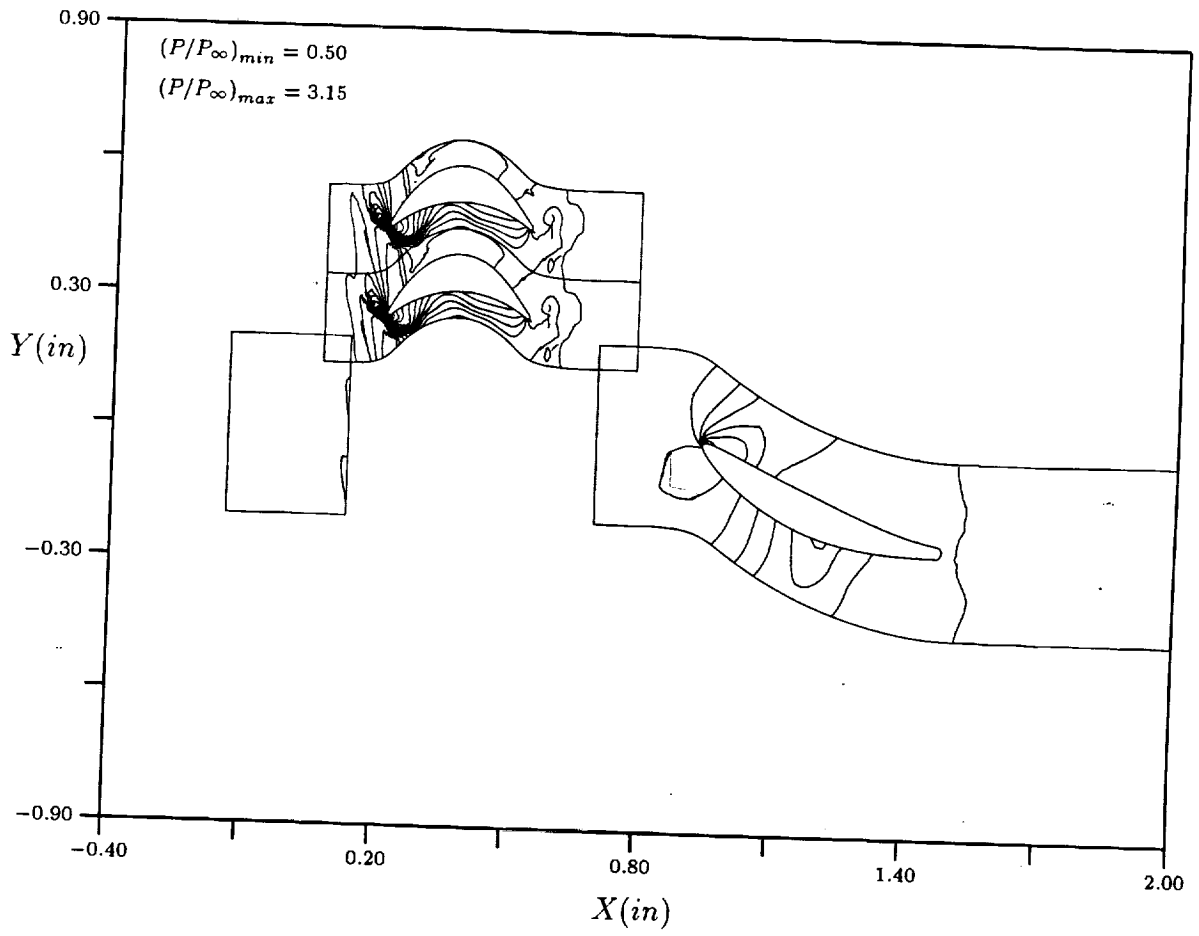
Figure 30: Static pressure contours at midspan - 60% cycle.

45

$(P/P_\infty)_{min} = 0.50$

$(P/P_\infty)_{max} = 3.15$
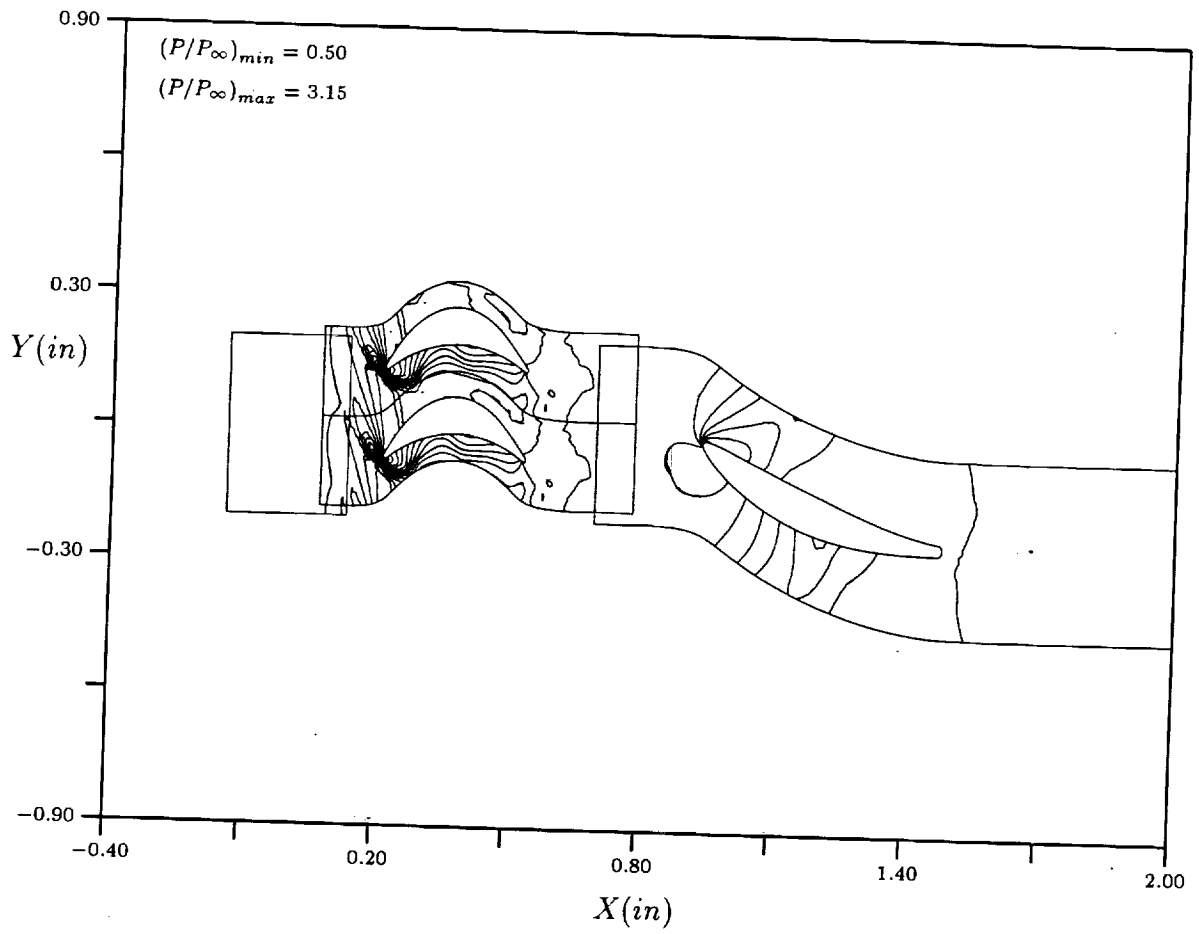
Figure 31: Static pressure contours at midspan - 80% cycle.

46
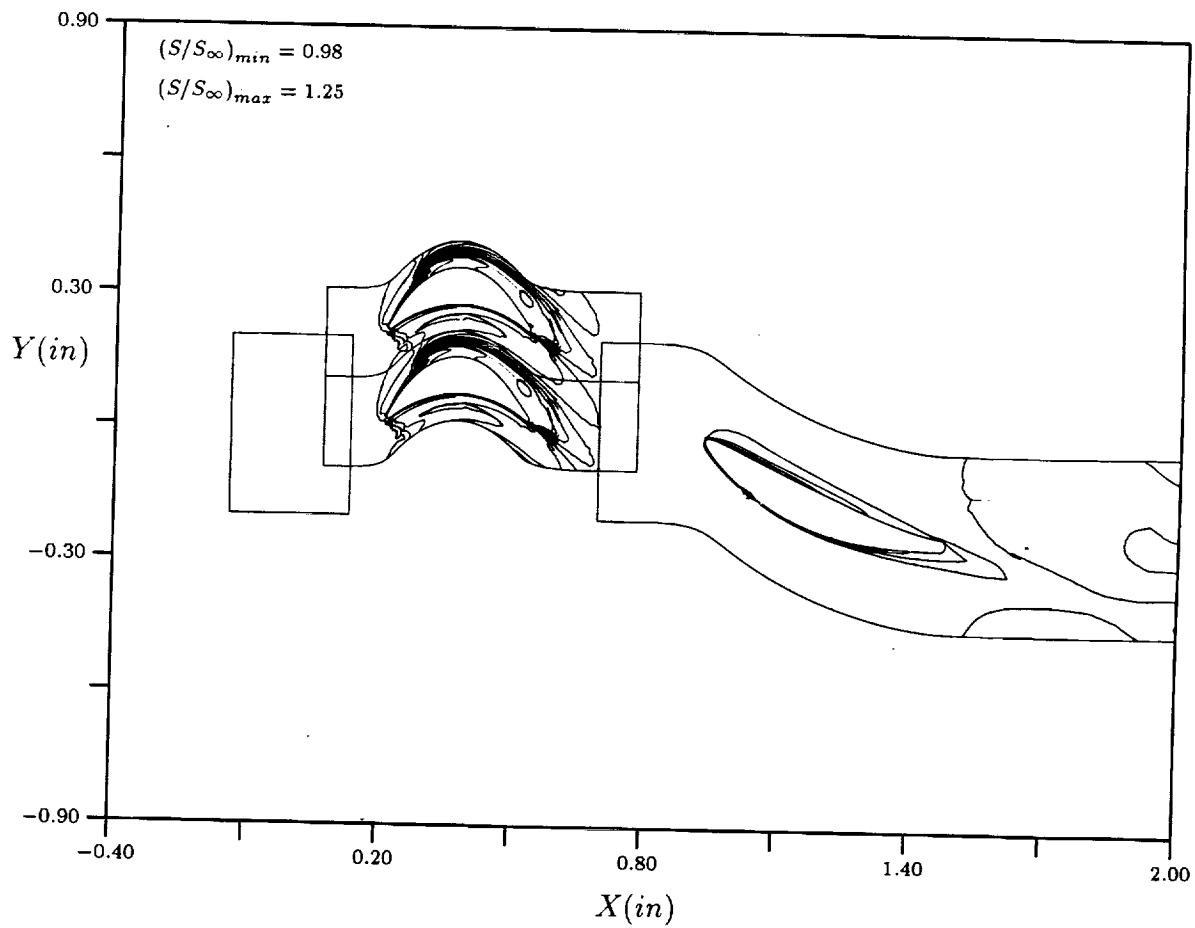
Figure 32: Entropy contours at midspan - 0% cycle.

$(S/S_\infty)_{min} = 0.98$

$(S/S_\infty)_{max} = 1.25$

Figure 33: Entropy contours at midspan - 20% cycle.

48

Figure 34: Entropy contours at midspan - 40% cycle.

49

Figure 35: Entropy contours at midspan - 60% cycle.

Figure 36: Entropy contours at midspan - 80% cycle.
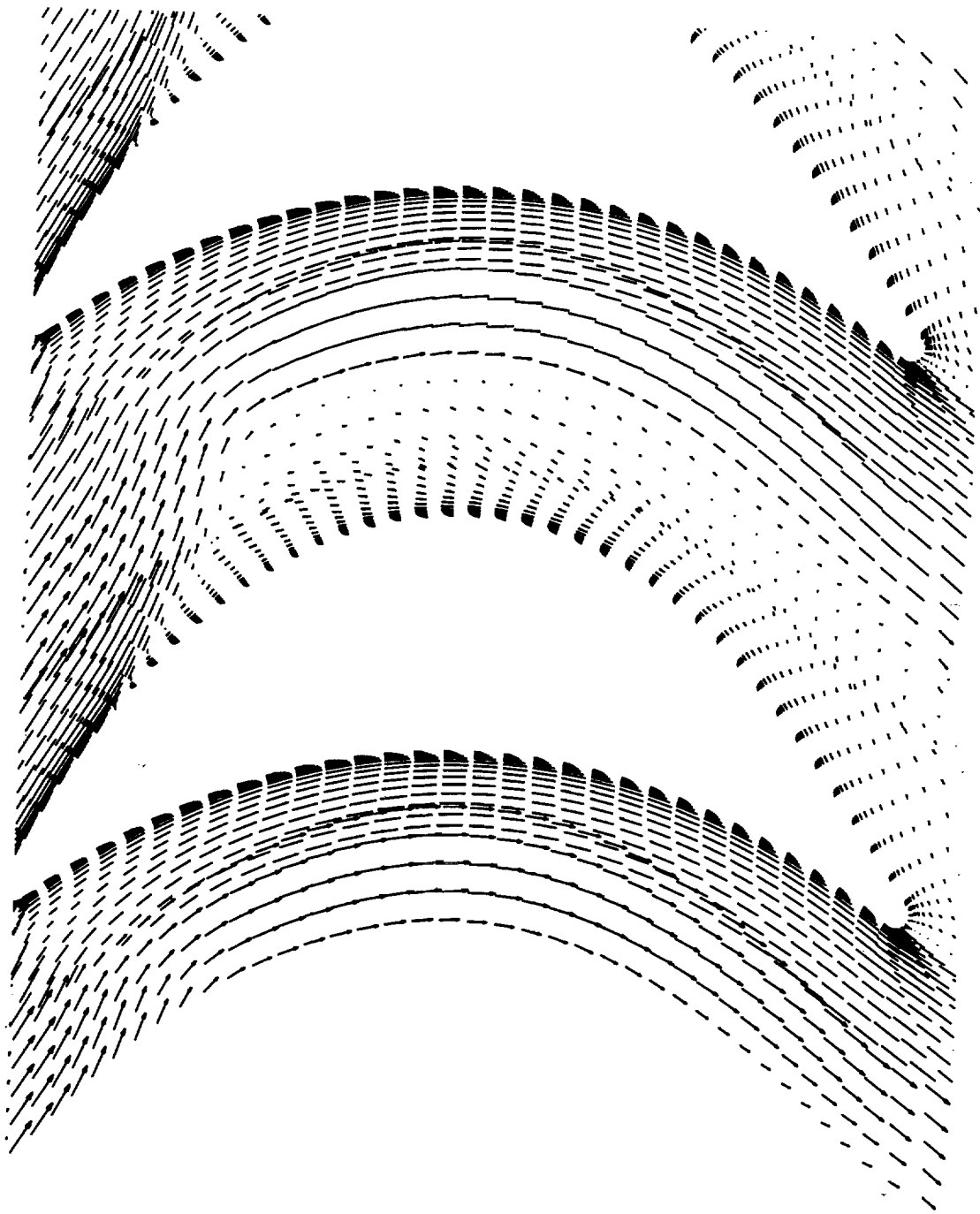
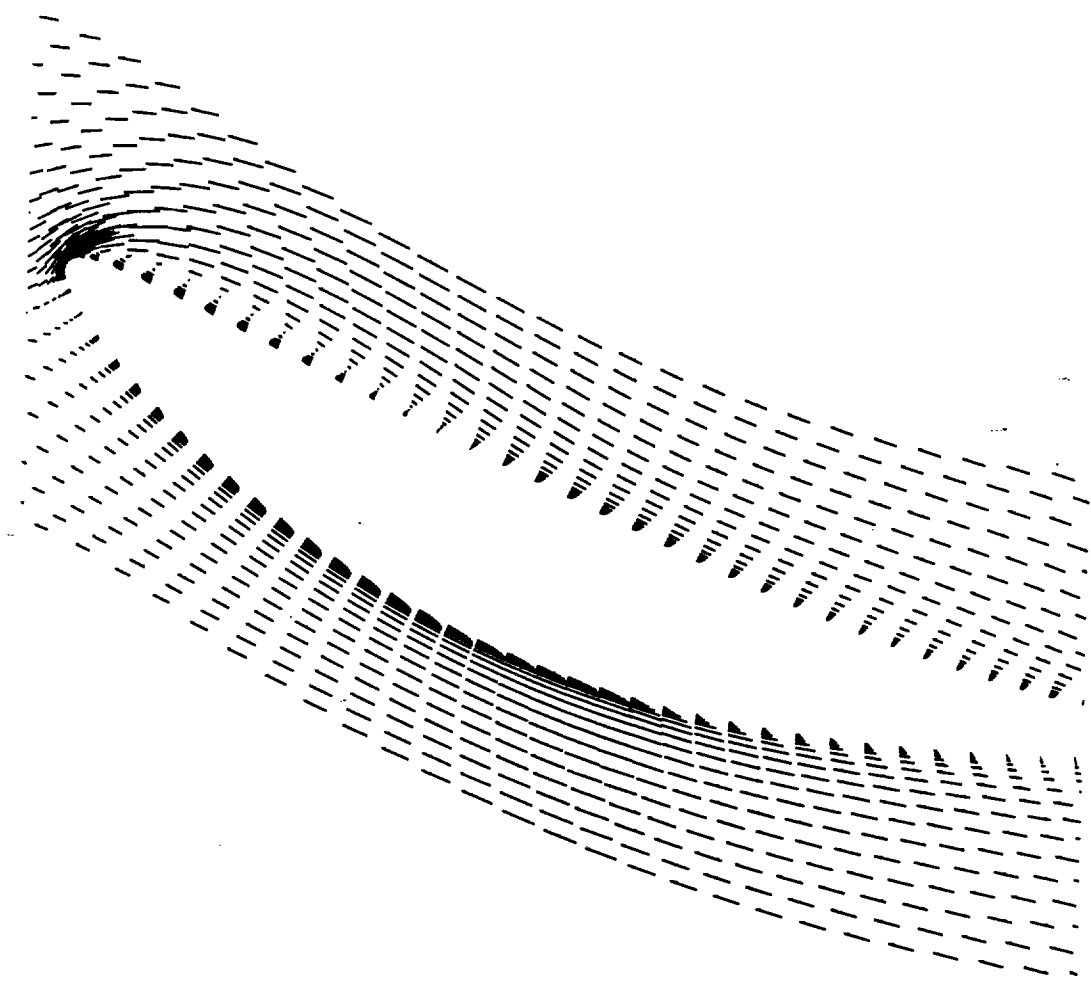Figure 37: Relative-frame velocity vectors in the rotor - 80% cycle.

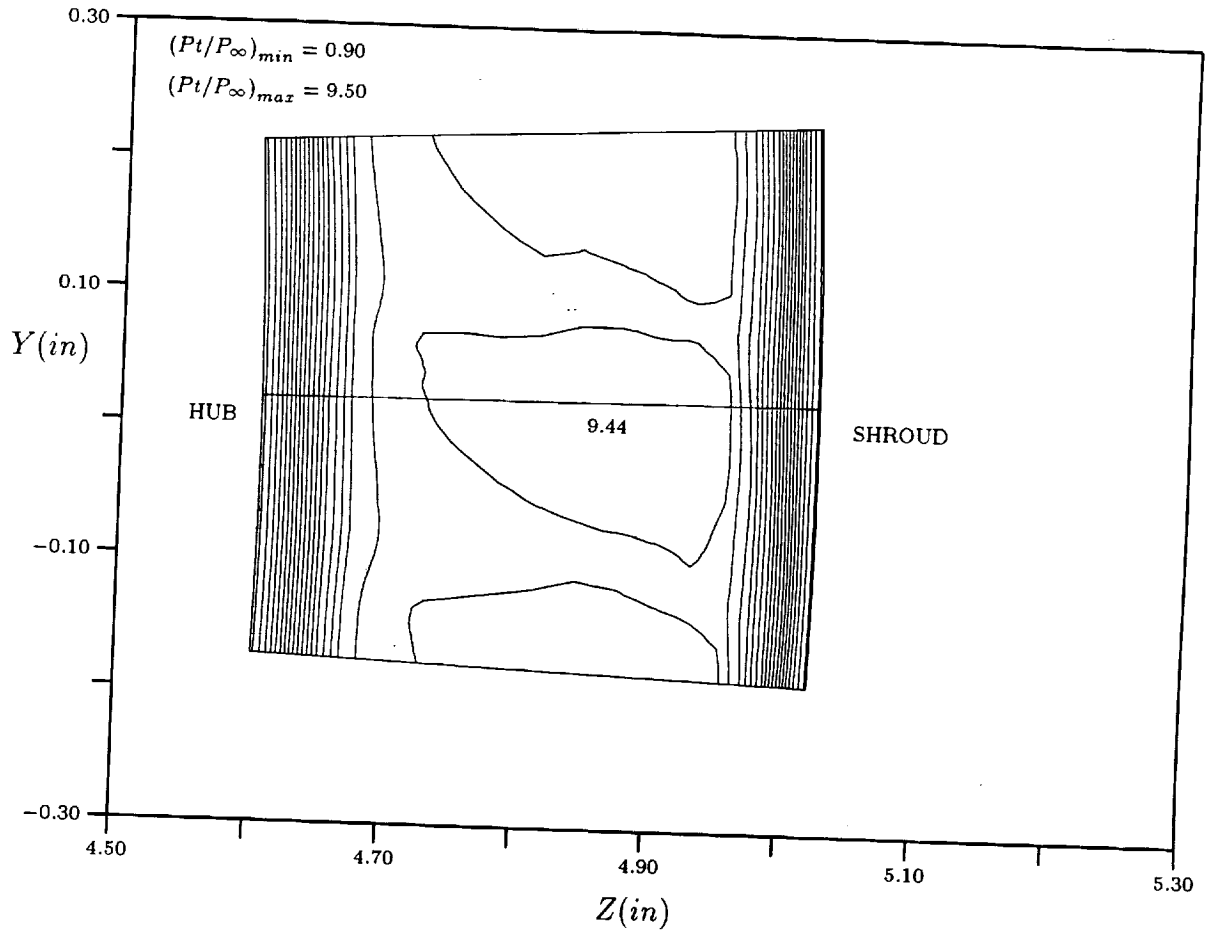Figure 38: Relative-frame velocity vectors in the vane - 80% cycle.

53

Figure 39: Total pressure contours 30% of the rotor axial chord upstream of the rotor - 80% cycle.
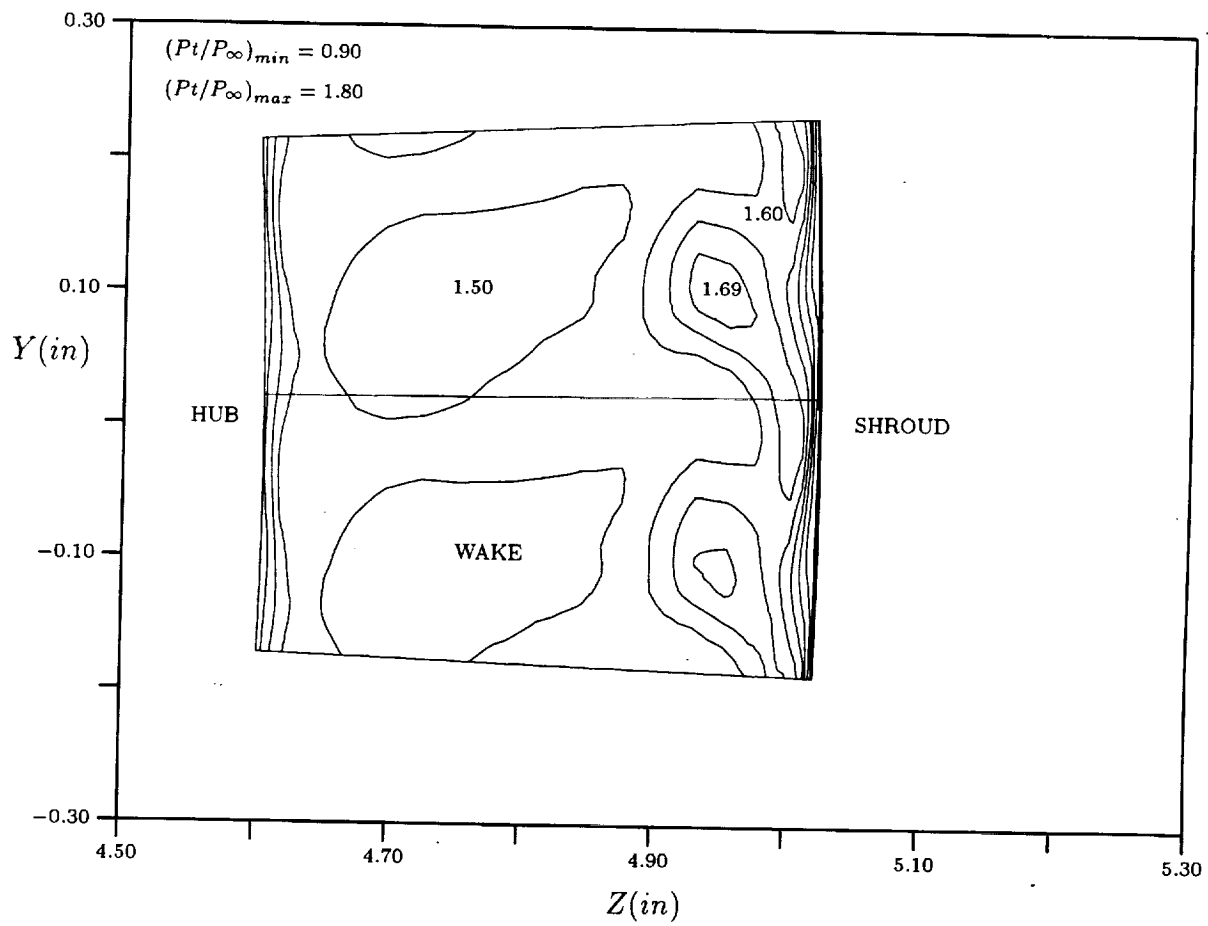
Figure 40: Total pressure contours midway between the rotor and vane - 80% cycle.
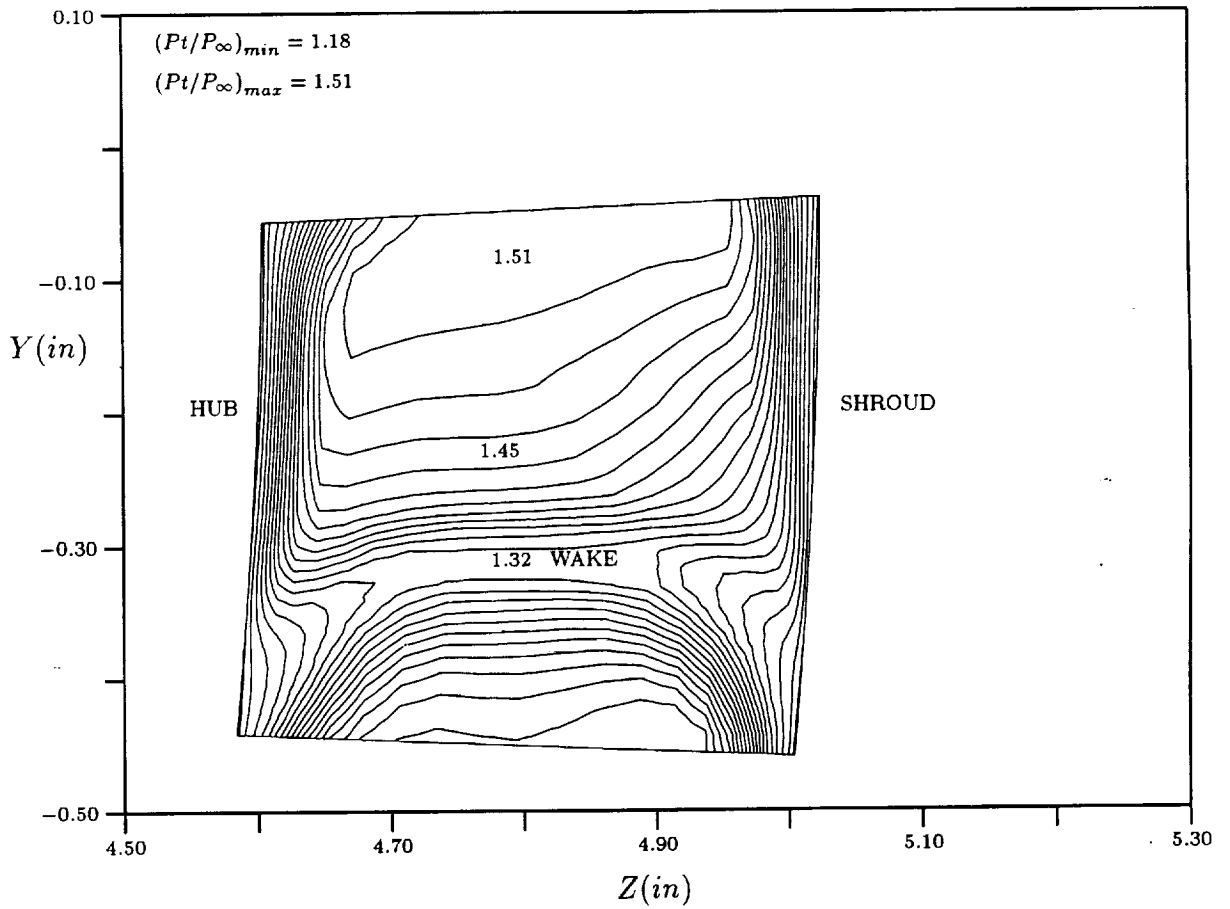
Figure 41: Total pressure contours 47% of the vane axial chord downstream of the vane - 80% cycle.